



Publication Year	2022
Acceptance in OA@INAF	2023-05-22T13:18:20Z
Title	Structure in the Magnetic Field of the Milky Way Disk and Halo Traced by Faraday Rotation
Authors	Dickey, John M.; West, Jennifer; Thomson, Alec J.M.; Landecker, T. L.; Bracco, A.; et al.
DOI	10.3847/1538-4357/ac94ce
Handle	http://hdl.handle.net/20.500.12386/34181
Journal	THE ASTROPHYSICAL JOURNAL
Number	940



Structure in the Magnetic Field of the Milky Way Disk and Halo Traced by Faraday Rotation

John M. Dickey¹, Jennifer West², Alec J. M. Thomson³, T. L. Landecker⁴, A. Bracco⁵, E. Carretti⁶, J. L. Han^{7,8,9}, A. S. Hill^{4,10}, Y. K. Ma¹¹, S. A. Mao¹², A. Ordog^{4,10}, Jo-Anne C. Brown¹³, K. A. Douglas^{4,13,14}, A. Erceg¹⁵, V. Jelić¹⁵, R. Kothes⁴, and M. Wolleben¹⁶

¹ School of Natural Sciences, Private Bag 37, University of Tasmania, Hobart, TAS, 7001, Australia; john.dickey@utas.edu.au

² Dunlap Institute for Astronomy and Astrophysics, University of Toronto, Toronto, ON M5S 3H4, Canada

³ CSIRO Space & Astronomy, P.O. Box 1130, Bentley, WA 6102, Australia

⁴ National Research Council Canada, Dominion Radio Astrophysical Observatory, P.O. Box 218, Penticton, British Columbia, V2A 6J9, Canada

⁵ Laboratoire de Physique de l'École Normale Supérieure, ENS, Université PSL, CNRS, Sorbonne Université, Université de Paris, F-75005 Paris, France

⁶ INAF—Istituto di Radioastronomia, Via Gobetti 101, I-40129 Bologna, Italy

⁷ National Astronomical Observatories, Chinese Academy of Sciences, A20 Datun Road, Chaoyang District, Beijing 100101, People's Republic of China

⁸ CAS Key Laboratory of FAST, NAOC, Chinese Academy of Sciences, People's Republic of China

⁹ School of Astronomy and Space Sciences, University of Chinese Academy of Sciences, Beijing 100049, People's Republic of China

¹⁰ Department of Computer Science, Math, Physics, and Statistics, University of British Columbia, Okanagan Campus, 3187 University Way, Kelowna, BC V1V1V7, Canada

¹¹ Research School of Astronomy & Astrophysics, Australian National University, Canberra, ACT 2611, Australia

¹² Max Planck Institute for Radio Astronomy, Auf dem Hügel 69, D-53121 Bonn, Germany

¹³ Department of Physics and Astronomy, University of Calgary, Calgary, AB T2N 1N4, Canada

¹⁴ Physics and Astronomy Department, Okanagan College, 1000 KLO Road, Kelowna, British Columbia, V1Y 4X8, Canada

¹⁵ Rudjer Bošković Institute, Bijenička cesta 54, 10 000 Zagreb, Croatia

¹⁶ Skaha Remote Sensing Ltd., 3165 Juniper Drive, Naramata, BC V0H 1N0, Canada

Received 2022 July 18; revised 2022 September 20; accepted 2022 September 22; published 2022 November 22

Abstract

Magnetic fields in the ionized medium of the disk and halo of the Milky Way impose Faraday rotation on linearly polarized radio emission. We compare two surveys mapping the Galactic Faraday rotation, one showing the rotation measures of extragalactic sources seen through the Galaxy, and one showing Faraday depth of the diffuse Galactic synchrotron emission from the Global Magneto-Ionic Medium Survey. Comparing the two data sets in $5^\circ \times 10^\circ$ bins shows good agreement at intermediate latitudes, $10^\circ < |b| < 50^\circ$, and little correlation between them at lower and higher latitudes. Where they agree, both tracers show clear patterns as a function of Galactic longitude, ℓ ; in the northern hemisphere a strong $\sin(2\ell)$ pattern; and in the southern hemisphere a $\sin(\ell + \pi)$ pattern. Pulsars with height above or below the plane $|z| > 300$ pc show similar ℓ dependence in their rotation measures. Nearby nonthermal structures show rotation measure shadows as does the Orion–Eridanus superbubble. We describe families of dynamo models that could explain the observed patterns in the two hemispheres. We suggest that a field reversal, known to cross the plane a few hundred parsecs inside the solar circle, could shift to positive z with increasing Galactic radius to explain the $\sin(2\ell)$ pattern in the northern hemisphere. Correlation shows that rotation measures from extragalactic sources are one to two times the corresponding rotation measure of the diffuse emission, implying Faraday complexity along some lines of sight, especially in the southern hemisphere.

Unified Astronomy Thesaurus concepts: Galaxy magnetic fields (604); Interstellar medium (847); Milky Way magnetic fields (1057); Milky Way Galaxy physics (1056); Milky Way Galaxy (1054); Milky Way disk (1050)

1. Introduction

The magnetoionic medium is a mixture of ionized interstellar gas and magnetic field (\mathbf{B}) that causes Faraday rotation of linearly polarized radiation at radio wavelengths. The ionized gas can be either in classical H II regions or in the diffuse ionized medium, in both the Milky Way disk and halo. Although only the line-of-sight (LoS) component of the \mathbf{B} field contributes to Faraday rotation, surveys of rotation measure (RM) provide such high precision and resolution that a useful picture of the interstellar magnetic field emerges (Han 2001, 2017; Brown et al. 2007; Van Eck et al. 2011; Beck 2015; Haverkorn 2015; Jaffe 2019).

To survey the RM requires a source of polarized emission, either compact sources or the diffuse synchrotron emission by cosmic-ray electrons in the Galactic \mathbf{B} field. Pulsars are excellent polarized sources, and the study of their RMs shows the structure of the ionized interstellar medium in the disk and lower halo (Han et al. 1999, 2006, 2018; Sobey et al. 2019), but it is limited by our imprecise knowledge of pulsar distance (Cordes & Lazio 2002; Gaensler et al. 2008; Yao et al. 2017). Most pulsars are close to the Galactic midplane, but a few are high enough above and below the plane that their RMs sample the magnetic field in the lower halo as well as in the disk. Extragalactic radio sources are often polarized, with intrinsic Faraday rotation that contributes to their RMs, but their measured RMs can be gridded, interpolated, and smoothed using a Bayesian inference scheme to determine the contribution due to the Galactic foreground as a smooth function, i.e., the Galactic foreground RM (Han et al. 1997, 1999; Oppermann et al. 2012;

Xu & Han 2014; Oppermann et al. 2015; Ferrière 2016; Hutschenreuter & Enßlin 2020; Hutschenreuter et al. 2022). For brevity we refer to the resulting values as the extragalactic RM, because it is based on surveys of polarized radio galaxies, but the gridded map is an estimate of the foreground, i.e., the Milky Way contribution to the RMs of the sources.

Another approach to measuring Galactic RMs is to study the Faraday spectrum of the diffuse Galactic synchrotron emission. The Faraday spectrum (Burn 1966; Brentjens & de Bruyn 2005; Wolleben et al. 2010; Lenc et al. 2016; Van Eck et al. 2019; Ferrière et al. 2021) shows how the polarized brightness is distributed over a range of values of Faraday depth, φ , corresponding to the RM of the intervening magnetoionic medium along the LoS between the telescope and each emission region. Since diffuse Galactic synchrotron emission is widespread along every LoS, the RM generalizes to the first moment of the Faraday spectrum (Dickey et al. 2019). In this study, we make use of the Global Magneto-Ionic Medium Survey (GMIMS) High-Band North (HBN) polarization data set (Wolleben et al. 2021), in particular its first moments, which we will loosely refer to as the GMIMS or diffuse RM.

Comparing Galactic and extragalactic RMs at centimeter wavelengths has been done in small areas, particularly at low latitudes, (Ordog et al. 2017, 2019; McKinven 2021) and in larger areas at low frequencies (Riseley et al. 2020; Erceg et al. 2022). Prior to GMIMS (Wolleben et al. 2021), large area surveys of the polarized synchrotron emission, e.g., Spoelstra (1984), Landecker et al. (2010), did not have sufficient bandwidth, i.e., range in λ^2 , to resolve the emission across the Faraday spectrum and allow accurate computation of the first moment of the RM. This RM comparison over the whole sky north of $\delta = -28^\circ$ is the first step in a series of papers that will exploit the GMIMS RMs to understand the distribution of the Galactic \mathbf{B} field with cosmic-ray electrons that generate the synchrotron emission.

Section 2 describes the RM data from the GMIMS survey and compares it to the extragalactic RMs. Section 3 discusses the pulsar RMs and models for the nearby disk field, and presents a spherical harmonic expansion of the RM survey results, with a discussion of the imprint of nearby synchrotron and $H\alpha$ emission regions. There we compare the RMs of samples of pulsars that are at different heights, z , above or below the midplane with the extragalactic and diffuse emission RMs. Section 4 asks whether the asymmetry between the two Galactic hemispheres might be consistent with current dynamo models that solve the plasma equations for the global disk and halo field. A combination of M0 and M1 dynamo solutions is promising and worth further study. Section 5 discusses the significance of the ratios between the corresponding RM values in the extragalactic and GMIMS data, as evidence for different distributions of magnetoionic (rotating) medium and synchrotron emission. Section 6 summarizes the results and suggests an overhead (positive z) field reversal as a possible paradigm for the RM pattern in the northern hemisphere.

2. Rotation Measure Surveys Compared

The extragalactic RM data used here is the map made from interpolation and gridding of RM catalogs by Hutschenreuter et al. (2022), successor to similar maps by Hutschenreuter & Enßlin (2020), Oppermann et al. (2012, 2015). RMs for the diffuse Galactic emission are derived from the GMIMS HBN survey (Wolleben et al. 2021) observed at wavelengths

between 17 and 23 cm with the DRAO 26 m telescope. The GMIMS RMs are the first moment of the Faraday cube (Dickey et al. 2019; Ordog 2020, Section 4.1). For pixels whose maximum polarized intensities in the Faraday cube are less than 0.03 K, the first moment is not computed, and the map is blanked. The GMIMS first-moment map is further blanked for declinations less than -25° , to avoid systematic effects near the southern horizon of the survey at $\delta = -30^\circ$.

To study the large-scale longitude variation of the RMs from the two data sets, we sacrifice angular resolution by binning the data into cells with sizes of a few degrees, then compute the median value and the dispersion of the values in each bin. This process reduces the scatter due to the small-scale structure in the RMs; the median filter attenuates the effect of spurious points with very large positive or negative RMs that may be caused by small regions of high electron density and/or a strong, localized, random component in the Galactic \mathbf{B} field. Many different bin sizes were tried, all giving qualitatively similar results, described in Appendix A. Here we present the profiles for bins with longitude width 10° and latitude width 5° . A reduced chi-squared measure of goodness of fit is given in Appendix B with a discussion of its limitations due to the non-Gaussian distribution of RM values in the bins. The values from the two surveys are taken at the same points in the maps after reprojection to a common Healpix¹⁷ projection ($N_{\text{side}} = 512$, nested). Each bin has ~ 50 to 140 independent values, depending on the latitude, since the beam size (FWHM) of the GMIMS observations is $\sim 40'$. The density of the extragalactic sources is $\sim 1.3 \text{ deg}^{-2}$ on average, but lower for the south celestial pole region.

2.1. Longitude Dependence of the RMs

The upper panel of Figure 1 shows the GMIMS HBN (DRAO) first-moment map (Wolleben et al. 2021), with a red outline showing the area influenced by the North Polar Spur (NPS; see Section 2.3 below) at midlatitudes. The lower panel of Figure 1 shows the Hutschenreuter et al. (2022) map based on extragalactic source RMs. The bin edges in longitude are spaced by 10° , indicated by the solid and dotted meridional lines in Figure 1. The dispersion of RM values in each bin is computed from the 16th and 84th percentiles of their distributions, corresponding to roughly $\pm 1\sigma$ for a Gaussian distribution. These are plotted as error bars on the data points in Figure 2.

Two examples of the median-filtered RM versus longitude data using latitudes $+35^\circ < b < +40^\circ$ and latitudes $+40^\circ < b < +45^\circ$ (marked by the green dashed lines in Figure 1) are shown in Figure 2. The GMIMS (DRAO) values are shown in blue; the extragalactic values are in red. The formulae indicated on the figure are least-squares fits to the points using a five-parameter function to determine the first three terms of a Fourier series in longitude, ℓ , i.e.,

$$\text{RM}(\ell) = C_0 + C_1 \sin(\ell + \phi_1) + C_2 \sin 2(\ell + \phi_2). \quad (1)$$

Values of the constants C_0 , C_1 , C_2 , ϕ_1 , and ϕ_2 , with errors, are given in Table 1 for the range of latitudes $-60^\circ < b < +60^\circ$. Errors on the parameters are the square roots of the diagonal elements of the covariance matrix, from SCIPY routine `optimize.curve_fit` (Virtanen et al. 2020). Amplitudes and phases

¹⁷ <http://healpix.sourceforge.net> (Górski et al. 2005).

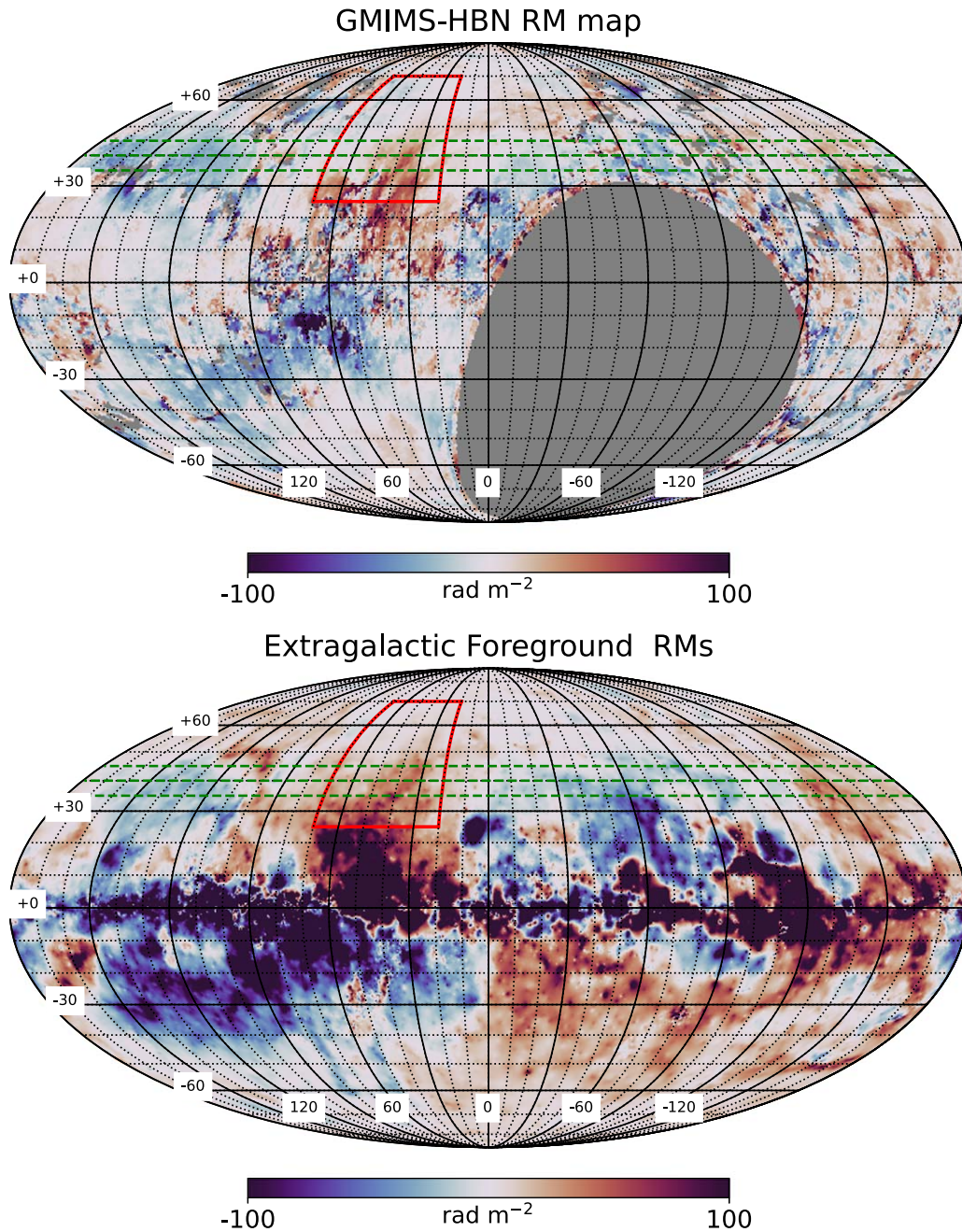


Figure 1. Two maps of the Galactic RM. The upper panel shows the GMIMS High-Band North first-moment map made with data from the DRAO 26 m telescope (Wolleben et al. 2021). The lower panel shows the Galactic estimate based on extragalactic source RMs (Hutschenreuter et al. 2022). The red box indicates the area dominated by the North Polar Spur in Stokes I synchrotron emission; see Section 2.3 below. The green dashed lines illustrate two sets of bins at constant latitude, used to make the two panels in Figure 2.

shown in bold face in Table 1 are statistically significant, either because the amplitude is more than five the error or because the phase error is less than 0.15 radians (8°) for ϕ_1 or 0.075 radians (4°) for ϕ_2 . The fitted phases have offsets of $\pm \pi$ so that all phases are in the ranges $-\pi < \phi_1 < +\pi$, and $-\frac{\pi}{2} < \phi_2 < +\frac{\pi}{2}$, and the amplitudes, C_1 and C_2 , are positive.

The values of the amplitudes and phases from Table 1 are displayed in Figure 3. The GMIMS phases and amplitudes are on the left panel, the extragalactic values are on the right panel, with phases at the top and amplitudes below. The amplitudes and phases of the $\sin(\ell)$ terms are shown in blue, of the $\sin(2\ell)$ terms in red. Some low-latitude points, ($|b| \leq 5^\circ$), are off scale

on the lower panels of Figure 3: to include them would collapse the scale so that the intermediate latitude points would be compressed at the bottom. At such low latitudes, the path lengths through the disk are very long, several kiloparsecs, so RMs can be very high, and they vary dramatically on angles smaller than the DRAO telescope beam. For the extragalactic RMs (right panel), the $\sin(\ell)$ term is much stronger than the $\sin(2\ell)$ term for negative latitudes, with the blue curve above the red for $b < 0^\circ$. For the GMIMS RMs, the negative latitudes are not fully sampled in longitude, so the amplitudes of the two terms are not well determined; all the GMIMS C_1 and C_2 values at $b < 0^\circ$ are less than 5σ in Table 1. The latitude range

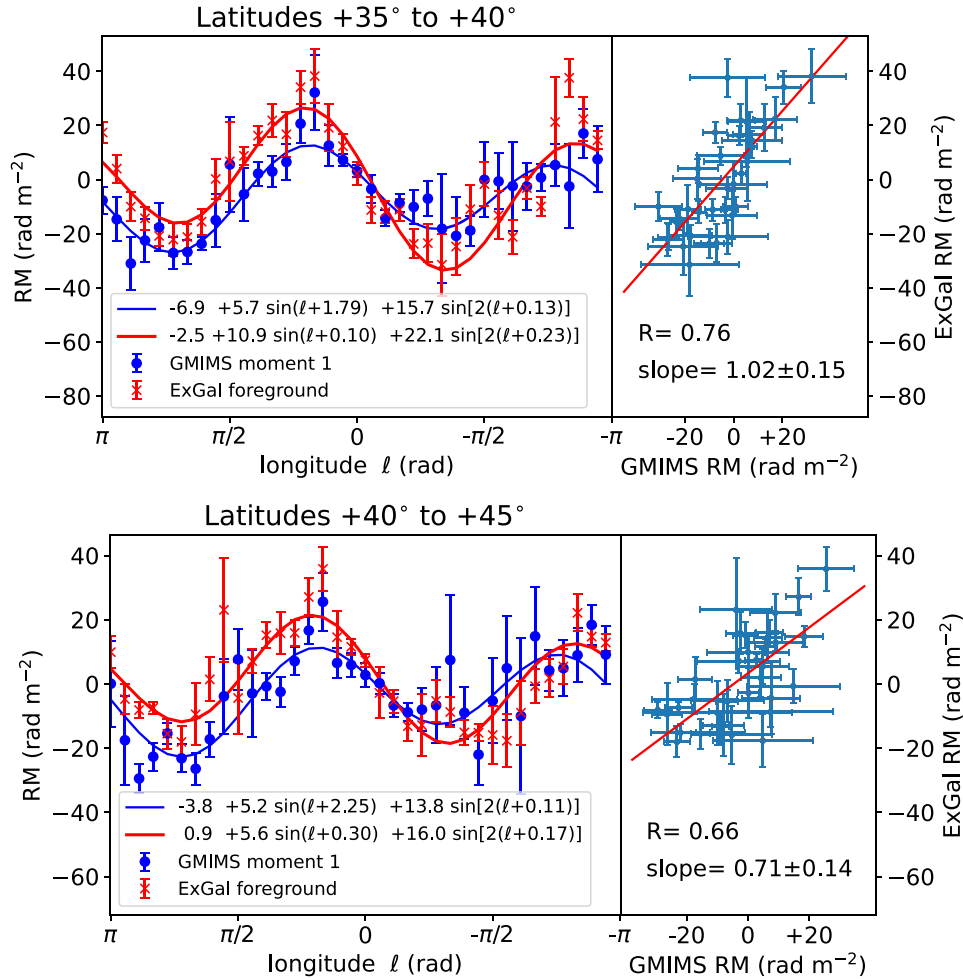


Figure 2. Examples of the $\sin(2\ell)$ form of the RM at intermediate positive latitudes. On the upper panel are profiles made from averaging the latitude range $+35^\circ < b < +40^\circ$, with the GMIMS (DRAO) data shown in blue and the extragalactic (ExGal) RM grid (Hutschenreuter et al. 2022) shown in red. Error bars on the points show $\pm 1\sigma$ of the distributions of values in each bin. The least-squares fit parameters are shown (Equation (1), see Table 1). In the lower panel is a similar pair of averages for $+40^\circ < b < +45^\circ$. In each panel, the scatter plot on the right shows the correlation between the median values from GMIMS (x-axis) and the extragalactic sample. The Pearson correlation coefficient (R) is indicated, along with the slope of the best linear fit, shown with the red line.

where $\sin(2\ell)$ dominates is $+20^\circ < b < +50^\circ$, where on the two lower panels the red curves are well above the blue in Figure 3.

For the latitude range $+20^\circ < b < +50^\circ$, all of the longitude slices of the extragalactic survey show fitted amplitudes C_2 in Table 1 that are greater than 5σ (4.9σ in one case) and also greater than C_1 , mostly by a factor of 2 or more. For all these latitudes, the fits show small errors in ϕ_2 , $\sigma_{\phi_2} \leq 0.08$ radians. These latitudes show similar domination by the $\sin(2\ell)$ term in the GMIMS data. All have values of C_2 from fits to the GMIMS data that are also above 5σ with the exception of $+25^\circ < b < +30^\circ$, where the C_2 value is at the 4.5σ level. The phases are well determined; the noise in the phase is $\sigma_{\phi_2} \leq 0.08$ radians.

2.2. Correlation Results

At high latitudes ($|b| > 50^\circ$), the RM values from the two surveys show little correlation. In both surveys, the RMs are close to zero at both poles, with means $+3.9$ and $+0.5 \text{ rad m}^{-2}$ for $50^\circ < b < 70^\circ$ for the extragalactic and GMIMS surveys, respectively. The standard deviations of the binned median RMs in this range are 6.5 rad m^{-2} for the GMIMS data and

2.4 rad m^{-2} for the extragalactic data. In the south, the GMIMS survey covers only about half of the high-latitude region. The GMIMS survey has a broad RM spread function (RMSF), $\delta\varphi = 140 \text{ rad m}^{-2}$ (Wolleben et al. 2021), as well as a large beam size ($\delta\theta = 40'$). The lack of correlation between the two surveys at high Galactic latitudes may be due in part to poor Faraday spectral resolution of the GMIMS data in an area of very small values of RM, to the low surface brightness of the diffuse polarized emission, and to the dominance of the random field component, as the projection of the ordered field on the LoS is small in this direction.

For latitudes between 20° and 50° , we plot a scatter diagram of the extragalactic versus GMIMS median RMs, calculated in the bins described above in the left panel of Figure 4. The correlation coefficient is $R = 0.69$, and the slope of the best-fit line is 1.1, using SCIPY regression analysis routine `stats.linregress`. In contrast, for latitudes above $b = +50^\circ$, there is no correlation; $R = -0.03$, as shown on the right panel of Figure 4. Values of R for each 5° of latitude are given in Table 2 and illustrated in Figure 5.

The negative latitudes all have a longitude range that is not sampled by the GMIMS survey (south of $\delta = -25^\circ$), so their scatter plots have fewer points, and the correlation tests only a

Table 1
Longitude Fit Parameters

Latitude Range ($^{\circ}$)	GMIMS (DRAO)					Extragalactic				
	C_o (rad m $^{-2}$)	C_1 (rad m $^{-2}$)	ϕ_1 (radians)	C_2 (rad m $^{-2}$)	ϕ_2 (radians)	C_o (rad m $^{-2}$)	C_1 (rad m $^{-2}$)	ϕ_1 (radians)	C_2 (rad m $^{-2}$)	ϕ_2 (radians)
$-60 < b < -55$	-15.5 ± 6.4	20.1 ± 10.0	-0.18 ± 0.15	12.9 ± 4.5	0.28 ± 0.09	8.1 ± 0.8	7.8 ± 1.2	2.99 ± 0.12	2.7 ± 1.0	0.65 ± 0.22
$-55 < b < -50$	-33.4 ± 10.8	47.2 ± 17.4	-0.31 ± 0.08	24.1 ± 7.2	0.35 ± 0.09	7.9 ± 0.9	10.9 ± 1.1	2.85 ± 0.13	3.2 ± 1.2	0.51 ± 0.22
$-50 < b < -45$	-29.1 ± 10.9	38.0 ± 17.1	-0.46 ± 0.13	25.5 ± 7.2	0.24 ± 0.10	5.2 ± 0.8	13.9 ± 1.2	2.73 ± 0.09	2.6 ± 1.2	0.85 ± 0.27
$-45 < b < -40$	-33.6 ± 6.4	44.3 ± 10.3	-0.42 ± 0.06	20.0 ± 4.6	0.33 ± 0.07	2.6 ± 1.3	19.0 ± 2.1	2.98 ± 0.09	6.3 ± 1.9	0.82 ± 0.15
$-40 < b < -35$	-20.9 ± 6.8	20.5 ± 10.0	-0.65 ± 0.19	17.2 ± 5.5	0.22 ± 0.11	-2.4 ± 2.1	31.7 ± 3.0	2.87 ± 0.09	12.1 ± 3.0	0.75 ± 0.11
$-35 < b < -30$	-12.5 ± 4.5	3.3 ± 7.9	-0.61 ± 0.74	13.1 ± 4.9	0.63 ± 0.11	-4.6 ± 2.5	40.3 ± 3.9	2.86 ± 0.08	5.0 ± 3.7	0.86 ± 0.32
$-30 < b < -25$	-16.3 ± 5.1	8.8 ± 7.6	-0.91 ± 0.56	19.6 ± 4.9	0.70 ± 0.09	-7.2 ± 3.0	53.1 ± 4.6	3.01 ± 0.07	13.5 ± 4.2	1.09 ± 0.14
$-25 < b < -20$	-14.4 ± 3.9	3.8 ± 3.2	-2.39 ± 1.69	15.5 ± 3.3	0.91 ± 0.15	-16.8 ± 3.6	57.0 ± 5.3	-3.13 ± 0.09	25.2 ± 5.4	1.01 ± 0.10
$-20 < b < -15$	-3.2 ± 6.3	11.6 ± 10.2	-2.93 ± 0.51	8.8 ± 4.2	1.09 ± 0.40	-13.4 ± 4.6	50.1 ± 6.8	-2.95 ± 0.12	29.6 ± 6.8	1.07 ± 0.10
$-15 < b < -10$	-4.0 ± 6.1	7.9 ± 9.4	-2.72 ± 1.06	1.4 ± 5.3	-0.11 ± 2.29	-9.2 ± 6.2	44.8 ± 9.3	-2.73 ± 0.18	32.0 ± 8.5	0.93 ± 0.14
$-10 < b < -5$	4.6 ± 4.7	24.7 ± 8.4	3.01 ± 0.16	9.8 ± 5.5	-1.30 ± 0.17	-2.3 ± 7.1	68.2 ± 10.7	-2.98 ± 0.14	12.4 ± 9.2	0.64 ± 0.36
$-5 < b < +0$	11.9 ± 4.8	29.9 ± 7.8	3.10 ± 0.20	9.3 ± 4.6	-1.09 ± 0.26	11.0 ± 11.4	100.9 ± 17.3	-3.09 ± 0.15	32.9 ± 14.4	0.06 ± 0.19
$+0 < b < +5$	-7.6 ± 4.3	21.1 ± 7.6	-0.81 ± 0.22	14.9 ± 5.1	0.30 ± 0.07	6.0 ± 13.3	44.1 ± 19.3	2.84 ± 0.43	78.3 ± 15.2	0.19 ± 0.10
$+5 < b < +10$	-11.6 ± 3.3	30.4 ± 6.2	-0.47 ± 0.10	23.7 ± 3.7	0.28 ± 0.04	19.4 ± 7.7	17.0 ± 9.2	1.75 ± 0.71	38.4 ± 8.7	0.25 ± 0.12
$+10 < b < +15$	1.5 ± 2.5	9.2 ± 3.7	-1.59 ± 0.49	13.2 ± 4.3	0.01 ± 0.08	12.3 ± 4.9	26.8 ± 7.9	0.19 ± 0.19	36.4 ± 6.0	0.14 ± 0.08
$+15 < b < +20$	-7.8 ± 3.7	19.6 ± 6.5	-0.17 ± 0.14	21.8 ± 3.6	0.32 ± 0.05	3.5 ± 3.1	30.7 ± 4.9	0.18 ± 0.12	27.2 ± 4.1	0.28 ± 0.08
$+20 < b < +25$	-10.2 ± 3.2	20.9 ± 5.1	-0.37 ± 0.13	22.9 ± 3.3	0.31 ± 0.05	3.6 ± 2.7	16.7 ± 3.8	0.23 ± 0.23	26.2 ± 3.4	0.25 ± 0.06
$+25 < b < +30$	-2.6 ± 2.6	8.3 ± 4.3	-0.13 ± 0.29	19.7 ± 3.1	0.16 ± 0.08	2.5 ± 1.9	14.8 ± 2.9	0.32 ± 0.16	27.9 ± 2.3	0.22 ± 0.04
$+30 < b < +35$	-5.3 ± 1.4	3.6 ± 2.2	-0.08 ± 0.60	16.5 ± 1.6	0.19 ± 0.07	2.0 ± 1.7	10.5 ± 2.7	-0.10 ± 0.19	23.2 ± 2.5	0.08 ± 0.05
$+35 < b < +40$	-6.9 ± 0.9	5.7 ± 1.3	1.79 ± 0.25	15.7 ± 1.2	0.13 ± 0.04	-2.5 ± 1.5	10.9 ± 2.3	0.10 ± 0.18	22.1 ± 2.4	0.23 ± 0.04
$+40 < b < +45$	-3.8 ± 1.3	5.2 ± 1.5	2.25 ± 0.39	13.8 ± 1.6	0.11 ± 0.07	0.9 ± 0.9	5.6 ± 1.4	0.30 ± 0.19	16.0 ± 1.3	0.17 ± 0.04
$+45 < b < +50$	-0.5 ± 1.3	6.2 ± 1.9	2.70 ± 0.19	10.6 ± 1.4	0.31 ± 0.08	4.1 ± 0.9	3.3 ± 1.4	0.06 ± 0.34	8.7 ± 1.5	0.30 ± 0.06
$+50 < b < +55$	0.5 ± 1.0	6.6 ± 1.5	2.75 ± 0.14	7.3 ± 1.4	0.66 ± 0.08	3.9 ± 0.7	1.1 ± 1.2	0.10 ± 0.96	6.1 ± 1.3	0.47 ± 0.08
$+55 < b < +60$	2.2 ± 1.0	4.7 ± 1.5	2.45 ± 0.25	4.6 ± 1.3	1.52 ± 0.15	6.4 ± 0.7	5.6 ± 0.9	-1.02 ± 0.18	0.6 ± 0.9	-0.26 ± 0.75

Note. Parameters from Equation (1), bold face indicates statistically significant values.

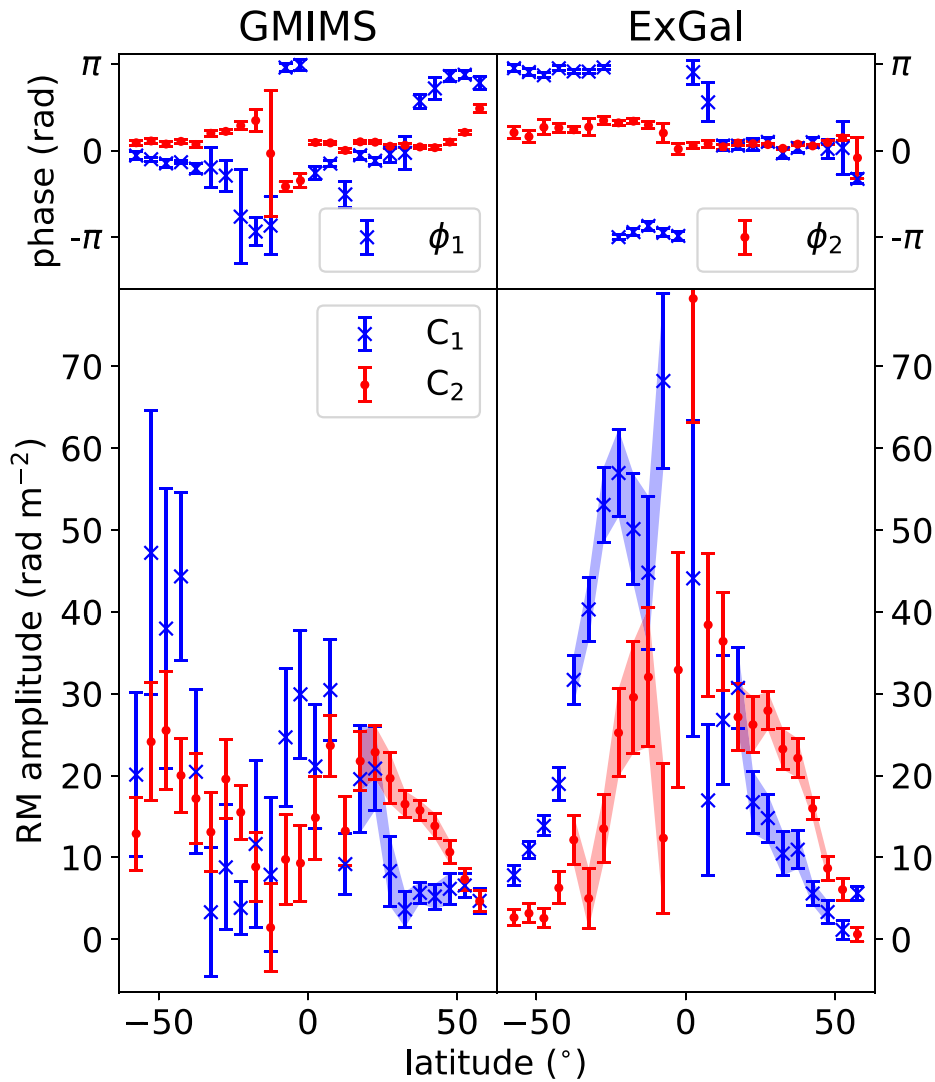


Figure 3. Amplitudes (C_1 and C_2) and phases (ϕ_1 and ϕ_2) of the $\sin(\ell)$ and $\sin(2\ell)$ terms, from Table 1. The GMIMS results are on the left, the extragalactic on the right. The values of the fitted parameters (Equation (1)) are shown in blue for the $\sin(\ell)$, and red for the $\sin(2\ell)$ terms. The curves are shaded for latitudes where the amplitudes, C_1 and/or C_2 , are greater than 5σ . At negative latitudes, much of the third and fourth quadrants are not observable in the GMIMS survey. Because of this, points on the left side of the left panel have large errors, and they are not shaded.

limited area. These R values are less secure. Even so, a pattern of correlation at midlatitudes emerges in both hemispheres, with little or no correlation at low latitudes ($-5^\circ < b < +5^\circ$) and at high latitudes ($|b| > 50^\circ$), illustrated in Figure 5. At midlatitudes in the southern hemisphere, most 5° strips show $R > 0.5$, with the exception of $-45^\circ < b < -40^\circ$ shown in Figure 6. So much of the longitude range is blanked in the GMIMS data that the fit results are not significant, as shown by the large spurious excursion in the fit in the unobserved region.

2.3. Effect of the North Polar Spur

The large angular-scale pattern of RMs at intermediate latitudes, which is apparent in the Galactic northern hemisphere as the $\sin(2\ell)$ pattern discussed here, has been ascribed to the effect of the NPS (Gardner et al. 1969; Lallement 2022; also called Loop I, in Section 3 below). It may be that the NPS is part of a larger structure that shapes the direction of the \mathbf{B} field throughout the hemisphere, a structure that could explain many large features in the synchrotron emission, optical and far-IR polarization, and cosmic-ray propagation (West et al. 2021). In

that case, the $\sin(2\ell)$ RM pattern may be a useful tracer of the direction of the LoS component of the field in this structure. On the other hand, if the effect of the NPS is restricted to the region of the first quadrant where the Stokes I emission shows a large loop (illustrated in Section 3), then it is worth checking whether the values of RM in these longitudes alone can cause the $\sin(2\ell)$ term to dominate over the $\sin(\ell)$ term, unlike in the southern hemisphere. To check, we blank the longitude range $20^\circ < \ell < 70^\circ$ for latitudes $+25^\circ < b < +70^\circ$, and repeat the analysis above. This area is shown by the red outlines in Figure 1. Blanking the NPS area gives results like those shown in Figure 7 and Table 3. The effect on the fitted amplitude and phase of the $\sin(2\ell)$ term of blanking the NPS in the first quadrant is small. All statistically significant values of C_2 and ϕ_2 (in bold face in Table 1) agree with their values for the unblanked maps within their errors, e.g., for latitudes $+35^\circ < b < +40^\circ$; C_2 is decreased from 15.7 ± 1.2 to 15.4 ± 1.4 rad m^{-2} for the GMIMS profile, and similarly from 22.1 ± 2.4 to 21.4 ± 2.6 rad m^{-2} for the extragalactic profile. The correlation between the two RM samples is reduced from $R = 0.76$ to $R = 0.64$. Comparing Figures 2 and 7 shows that

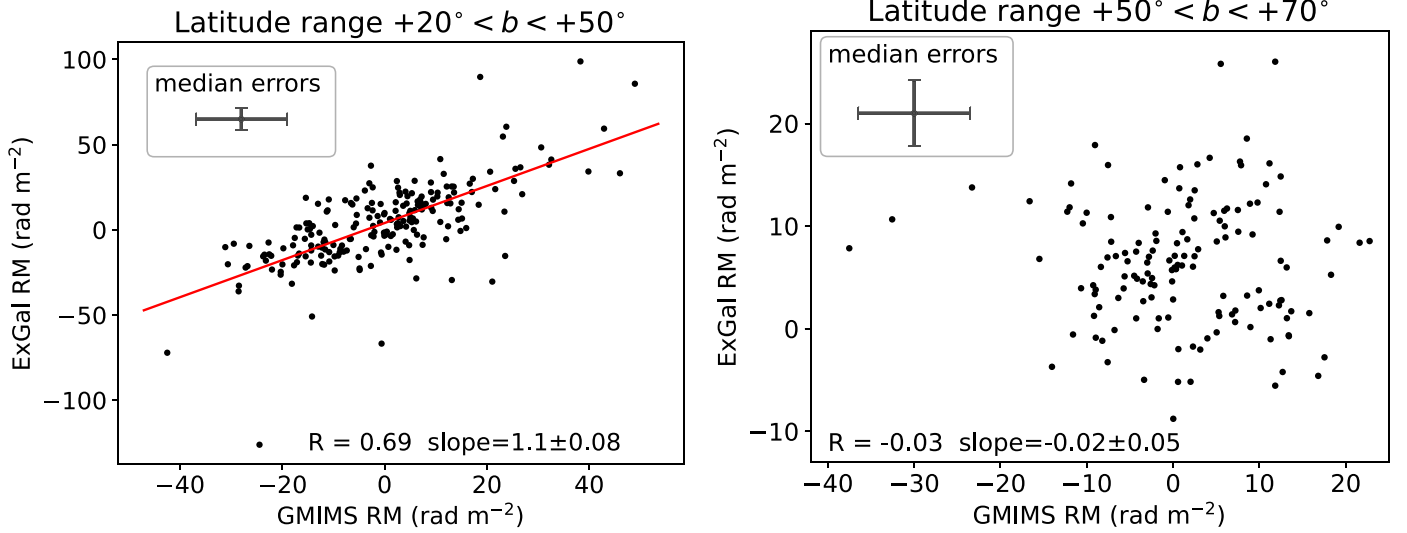


Figure 4. Scatter plots of median values from the extragalactic RM map of Hutschenreuter et al. (2022) vs. corresponding median values of RM from the GMIMS survey for the latitude range $+20^\circ < b < +50^\circ$ (left panel) and $+50^\circ < b < +70^\circ$ (right panel). On the left, the correlation coefficient is $R = 0.69$, and the slope of the best-fit line is 1.1 ± 0.08 , whereas on the right there is no correlation ($R = -0.03$). The median errors on the points are shown in the insets (high latitudes), the standard deviation of the GMIMS values is 9.8 (x -axis), and for the extragalactic values, the standard deviation is 6.1 (y -axis).

Table 2
Correlation Results

Latitude	R	Slope
$-60 < b < -55$	-0.11	-0.16 ± 0.35
$-55 < b < -50$	-0.11	-0.20 ± 0.43
$-50 < b < -45$	0.49	0.48 ± 0.19
$-45 < b < -40$	0.11	0.19 ± 0.39
$-40 < b < -35$	0.69	2.04 ± 0.49
$-35 < b < -30$	0.59	1.68 ± 0.51
$-30 < b < -25$	0.73	1.77 ± 0.37
$-25 < b < -20$	0.63	1.99 ± 0.54
$-20 < b < -15$	0.63	1.95 ± 0.53
$-15 < b < -10$	0.65	1.68 ± 0.42
$-10 < b < -5$	0.66	4.01 ± 0.98
$-5 < b < +0$	0.36	2.90 ± 1.58
$+0 < b < +5$	-0.02	-0.26 ± 2.59
$+5 < b < +10$	0.26	1.45 ± 1.10
$+10 < b < +15$	0.61	2.04 ± 0.54
$+15 < b < +20$	0.57	1.53 ± 0.44
$+20 < b < +25$	0.77	1.62 ± 0.26
$+25 < b < +30$	0.83	1.17 ± 0.15
$+30 < b < +35$	0.80	1.06 ± 0.14
$+35 < b < +40$	0.76	1.02 ± 0.15
$+40 < b < +45$	0.66	0.71 ± 0.14
$+45 < b < +50$	0.52	0.56 ± 0.16
$+50 < b < +55$	0.40	0.37 ± 0.15
$+55 < b < +60$	-0.42	-0.25 ± 0.09

the highest peaks in both profiles are in the blanked area, but the $\sin(2\ell)$ shapes are not significantly diminished when those peaks are removed. We conclude that the NPS does not by itself generate the $\sin(2\ell)$ pattern in the northern Galactic hemisphere. In the following sections, the NPS area is not blanked, but similar results are found if the blanking is applied.

2.4. Slopes, Amplitude Ratios, and Phases

There are many reasons why surveys of RMs with different telescopes may give different, even uncorrelated, results. Differences in the u, v plane coverage for different instruments

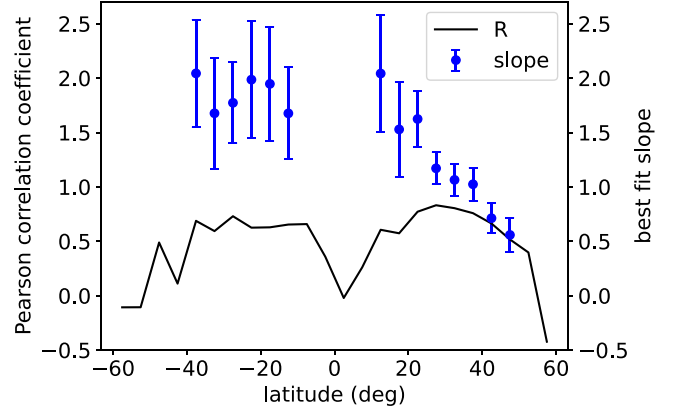


Figure 5. The Pearson correlation coefficient, R , vs. Galactic latitude, from Table 2. The blue dots show the slope, $\frac{\Delta RM_{\text{ExGal}}}{\Delta RM_{\text{GMIMS}}}$, of the best-fit line (right-hand axis). Dots are plotted only for latitudes $10^\circ < |b| < 50^\circ$ where the correlation is strong ($R > 0.5$).

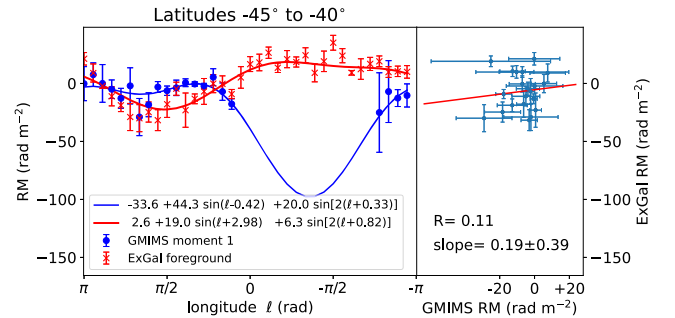


Figure 6. Comparison of GMIMS and extragalactic RMs at latitudes $-45^\circ < b < -40^\circ$. In this case, the two surveys give roughly similar results in the first and second Galactic quadrants ($0 < \ell < \pi$), but the GMIMS survey misses most of the third and fourth quadrants. The fitting is poorly constrained as a result, and the constants are ill determined. In addition, there is very little correlation between the RMs from the two surveys (right panel).

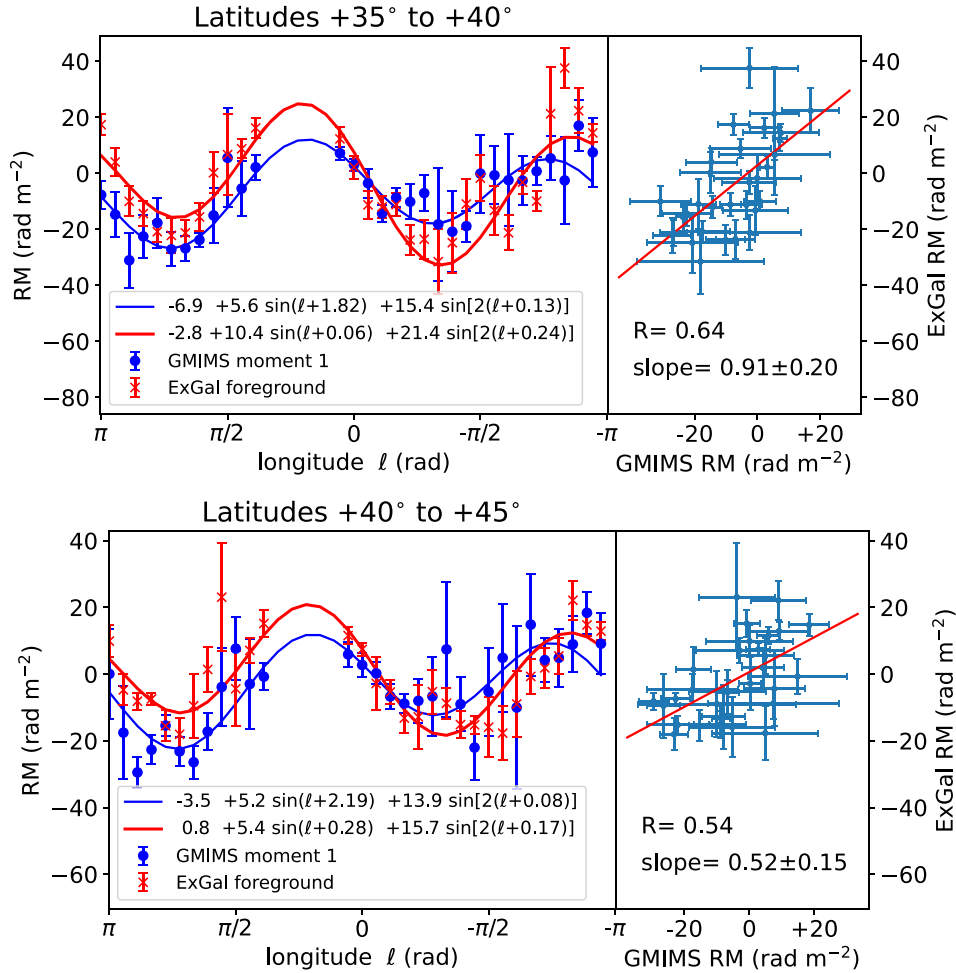


Figure 7. The effect of blanking an area that covers the bright emission region corresponding to the North Polar Spur ($25^\circ < b < 70^\circ$, and $20^\circ < \ell < 70^\circ$). The latitude ranges are the same as those shown in Figure 2.

leads to different angular resolution and spatial filtering of the polarized brightness distribution on the sky. In particular, single-dish surveys of diffuse polarization like GMIMS suffer from depolarization due to several physical effects that do not apply to observations of compact, extragalactic sources. Two very significant processes are beam depolarization and depth depolarization (Burn 1966; Tribble 1991; Sokoloff et al. 1998; Dickey et al. 2019). The large beam of the DRAO telescope blends together the emission from a large enough area that the polarized flux with many different position angles averages so as to attenuate the measured polarized intensity. This is particularly problematic at low Galactic latitudes where the polarization angle varies rapidly with the position on the sky. The extragalactic sources used to construct the RM grid are compact enough (a few arcseconds to tens of arcseconds) that variations in the foreground Galactic RM are too small to cause much beam depolarization, except where H II regions or another small-scale RM structure causes polarization shadows (Stil & Taylor 2007; Harvey-Smith et al. 2011; Thomson et al. 2019).

Depth depolarization of the diffuse Galactic emission occurs when synchrotron emission and Faraday rotation coexist within the same volume. Emission arising at different depths along the LoS suffers different rotation, and vector averaging reduces the observed polarized intensity. In the

simplest case, where magnetic field, synchrotron emissivity, and electron density are constant, the RM of the diffuse emission is exactly half that of an extragalactic source seen through the region (Burn 1966). If the ionized gas that causes the Faraday rotation is all in front of the diffuse polarized Galactic emission, there is no depth depolarization, and the extragalactic RM and the diffuse RM will be the same. If the synchrotron emission is in front of most of the rotating medium, there will be little or no correlation between the extragalactic and diffuse RMs.

Figure 8 plots the slopes determined from the regression analysis in Section 2.2, for only those latitudes having correlation coefficient $R > 0.5$, as in Figure 5. Also plotted in red is the ratio of the amplitudes of the $\sin(2\ell)$ terms of the extragalactic sample divided by the GMIMS amplitude, i.e.,

$$C_2 \text{ ratio} = \frac{C_{2-\text{ExGal}}}{C_{2-\text{GMIMS}}}. \quad (2)$$

Red points are plotted only for the latitudes having amplitudes for both extragalactic and GMIMS data greater than 5σ (with one exception each, as noted in the caption; see Table 1). These criteria select only $-40^\circ < b < -10^\circ$ and $+10^\circ < b < +50^\circ$ for the slopes, and $+15^\circ < b < +45^\circ$ for the amplitude ratios. All the southern hemisphere slopes are consistent with a value of 2 (the upper blue line in Figure 8), the maximum expected from a

Table 3
Fit Parameters with North Polar Spur Blanked (Equation (1))

Latitude Range (°)	GMIMS (DRAO)					Extragalactic				
	C_o (rad m ⁻²)	C_1 (rad m ⁻²)	ϕ_1 (radians)	C_2 (rad m ⁻²)	ϕ_2 (radians)	C_o (rad m ⁻²)	C_1 (rad m ⁻²)	ϕ_1 (radians)	C_2 (rad m ⁻²)	ϕ_2 (radians)
+25 < b < +30	-3.5 ± 1.9	5.4 ± 2.8	-0.56 ± 0.48	15.1 ± 2.7	0.16 ± 0.08	3.0 ± 2.0	15.8 ± 3.2	0.39 ± 0.15	28.7 ± 2.5	0.23 ± 0.04
+30 < b < +35	-5.7 ± 1.3	3.3 ± 2.0	-0.42 ± 0.58	15.8 ± 1.5	0.24 ± 0.07	1.2 ± 1.7	9.0 ± 2.7	-0.20 ± 0.22	21.4 ± 2.6	0.09 ± 0.05
+35 < b < +40	-6.9 ± 1.0	5.6 ± 1.3	1.82 ± 0.27	15.4 ± 1.4	0.13 ± 0.05	-2.8 ± 1.5	10.4 ± 2.5	0.06 ± 0.20	21.4 ± 2.6	0.24 ± 0.05
+40 < b < +45	-3.5 ± 1.4	5.2 ± 1.5	2.19 ± 0.43	13.9 ± 1.8	0.08 ± 0.07	0.8 ± 0.9	5.4 ± 1.4	0.28 ± 0.18	15.7 ± 1.3	0.17 ± 0.04
+45 < b < +50	-0.1 ± 1.3	6.0 ± 2.0	2.74 ± 0.26	10.1 ± 1.7	0.24 ± 0.09	4.7 ± 1.0	4.4 ± 1.5	0.16 ± 0.26	9.0 ± 1.4	0.26 ± 0.06
+50 < b < +55	1.6 ± 1.1	5.2 ± 1.4	2.39 ± 0.31	7.3 ± 1.5	0.52 ± 0.10	5.8 ± 0.9	3.8 ± 1.4	0.42 ± 0.28	7.2 ± 1.3	0.33 ± 0.07
+55 < b < +60	1.9 ± 1.4	4.8 ± 1.9	2.56 ± 0.36	5.1 ± 1.8	1.53 ± 0.16	6.6 ± 0.8	5.6 ± 0.9	-0.97 ± 0.21	1.1 ± 1.1	-0.26 ± 0.46

Note. Bold face indicates statistically significant values.

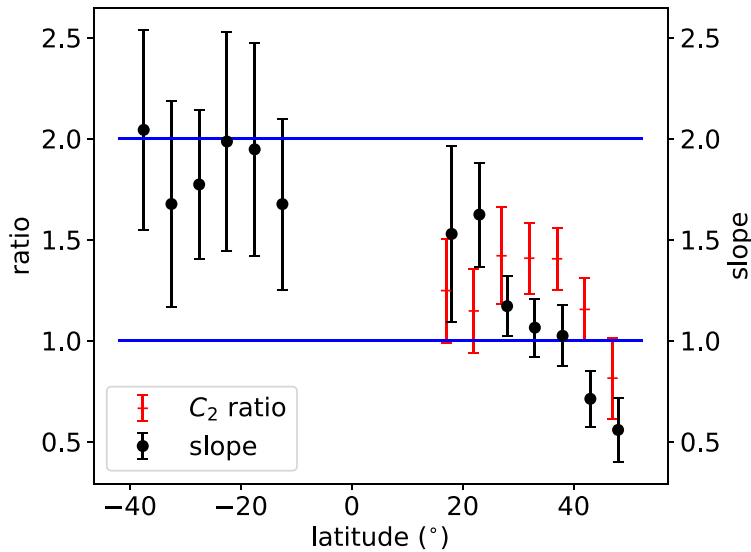


Figure 8. Correlation slopes and amplitude ratios for the $\sin(2\ell)$ terms at midlatitudes. Slopes are plotted for latitudes having $R > 0.5$ only. Amplitude ratios are plotted only for $+15 < b < +50$, for which all but one of the values of C_2 are greater than 5σ in both surveys. (The exceptions are latitudes 25° – 30° in the GMIMS survey that have $C_2 = 18.0 \pm 4.0 \text{ rad m}^{-2}$, i.e., 4.5σ , and latitudes 45° – 50° in the extragalactic survey that have $C_2 = 7.9 \pm 1.6 \text{ rad m}^{-2}$, i.e., 4.9σ .) The blue lines indicate the range of slopes expected for a uniform, Faraday thin slab. Values above 2 can arise in various ways, e.g., the diffuse emission is beginning to show depth depolarization. Values close to 1 suggest that the diffuse emission is behind most of the magnetoionic medium that causes the Faraday rotation in the extragalactic sample. A field reversal along the line of sight could explain values of the slope less than 1.

uniform slab of mixed emission and rotating medium. This suggests that the southern midlatitudes have polarized emission and Faraday rotation distributed mostly together along the LoS. On the other hand, the northern hemisphere points have lower values of the slopes, with values dropping from 1.62 to 0.56 as the latitude increases over the range $+15^\circ < b < +50^\circ$ approaching and passing the lower-limit value of 1 for foreground rotation (the lower blue line in Figure 8). In this case, the diffuse polarized emission and the extragalactic sources are on average showing roughly the same RMs, suggesting that the synchrotron emission is farther away than the medium that causes the Faraday rotation (Section 3.1 below). The amplitude ratios suggest an intermediate result for the component of the RMs that is modulated by the $\sin(2\ell)$ pattern. All of the red points are between 1 and 2 in Figure 8, suggesting that the synchrotron emission and the Faraday rotation are coextensive over part of the LoS, but with some background emission that is beyond the rotating medium.

The phases of the fitted functions, ϕ_1 and ϕ_2 in Equation (1), show good consistency in the intermediate latitude ranges where the fits show either a strong $\sin(2\ell)$ term (the northern Galactic hemisphere) or a strong $\sin(\ell)$ term (the southern Galactic hemisphere) as indicated by the shaded regions in Figure 3. But there is an offset of roughly π between ϕ_1 and ϕ_2 . Using the Pearson correlation coefficient $R > 0.5$ as a filter, and plotting only ϕ_2 values with error less than 0.075 radians ($=4''3$), gives the points on the right side of Figure 9. On the left are values of ϕ_1 with corresponding errors less than 0.15 radians. In the southern hemisphere, only the extragalactic survey has sufficient longitude coverage to give good fits in Equation (1). The fact that the phases of the $\sin(2\ell)$ terms in the north are close to zero, $0^\circ < \phi_2 < 20^\circ$, suggests that the field sampled by these RM surveys is nearly aligned, either parallel or perpendicular, to the direction to the Galactic center. If the large angular-scale pattern in the northern midlatitude

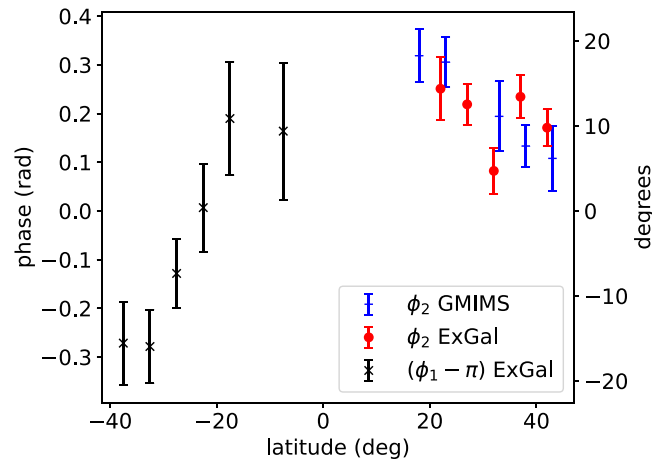


Figure 9. The fitted phases of the $\sin \ell$ and $\sin(2\ell)$ functions, i.e., ϕ_1 and ϕ_2 in Equation (1). In the northern hemisphere, ϕ_2 from both the GMIMS and the extragalactic fits are shown, in blue and red respectively. In the south, the extragalactic fits give $\phi_1 \approx \pi$. In the figure, we subtract π to get the black points on the same scale as the ϕ_2 values in the north. Note that both the error bars and the range of values for ϕ_1 naturally have about twice the range as for ϕ_2 because of the factor of 2 in the third term on the right of Equation (1). The conditions for including points on the plot are that $R > 0.5$ and the error in ϕ is small, i.e., $\sigma_{\phi_2} < 0.075$ radians or $\sigma_{\phi_1} < 0.15$ radians.

RMs is due primarily to a few nearby, large structures, then this alignment would be fortuitous. Thus Figure 9 strengthens the case for a global field configuration as the cause of the longitudinal modulation in the RMs, as discussed in Section 4 below. The close alignment of the zero phase direction in both the northern hemisphere $\sin(2\ell)$ and the southern hemisphere $\sin(\ell + \pi)$ functions with the Galactic center direction ($\ell = 0^\circ$) suggests that these patterns are both aligned by a global field pattern, e.g., an azimuthal or spiral field. The smooth decrease in ϕ_2 with increasing latitude in the north is suggestive of a transition between disk-dominated and halo-dominated fields,

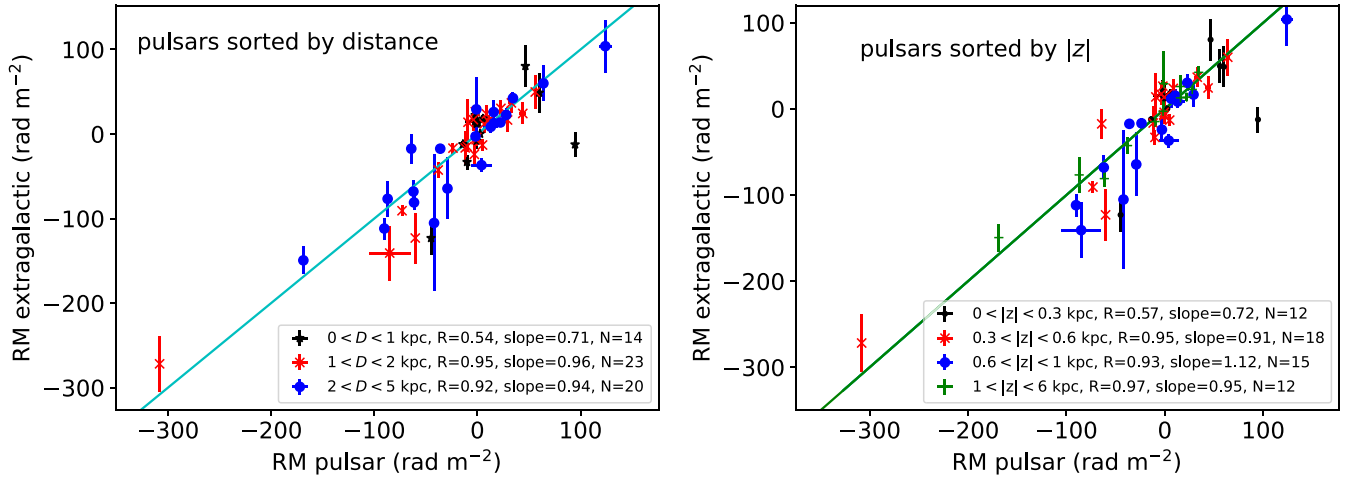


Figure 10. Scatter plots between rotation measures (RM) of Galactic pulsars with $10^\circ < |b| < 50^\circ$ taken from the ATNF catalog and RMs of extragalactic sources from Hutschenreuter et al. (2022). The scatter plots are organized by distance (D , left panel) and height above and below the Galactic plane ($|z|$, right panel). On the right panel, there is a tight correlation for pulsars with $|z| > 0.6$ kpc, as indicated by the Pearson coefficients, R , shown along with the number of pulsars in each sample, N , and the slope of the best-fit line, which approaches 1 as z increases. These numbers are summarized in Table 4. The pulsar RMs are very precisely measured; in most cases, the error bars are smaller than the symbols. The errors in the extragalactic RMs are the standard deviations in the Hutschenreuter et al. (2022) map at the positions of the pulsars.

or perhaps the effect of flow in or out of the disk (Henriksen & Irwin 2021).

3. Contributions to the RM at Intermediate Latitudes from the Nearby Disk

The distinct, contrasting patterns in the RM at intermediate latitudes in the northern and southern hemispheres, described above, trace the magnetic field and the diffuse ionized medium along the entire LoS through the Galaxy, for the extragalactic sources, or along the LoS to and through the synchrotron emission, for the GMIMS survey. Knowing the distances to the regions where most of the rotation takes place would help to interpret these patterns in terms of the magnetic field configuration. In particular, the contributions to the RMs due to electrons and magnetic field in the disk versus the halo of the Galaxy need to be distinguished (Mao et al. 2012). Distances to the sources of polarized radiation are needed in order to model the LoS distribution of the rotating medium, and to subtract the contribution of the nearby disk from the RMs at midlatitudes.

Pulsars are useful for tracing the three-dimensional distribution of RMs because their distances can be measured, either approximately by their dispersion measure (DM) or more precisely by parallax. Large samples of pulsar RMs (Han et al. 1999, 2006, 2018; Sobey et al. 2019) have been used to develop models of the field in the disk, (e.g., Han & Qiao 1994; Indrani & Deshpande 1999; Sun et al. 2008; Sun & Reich 2010; Van Eck et al. 2011; Jansson & Farrar 2012; Xu & Han 2019), and to estimate the scale heights of both the magnetic field and the diffuse electron layers. In this section, we consider the contribution to the RM by the medium in the nearby disk, based on several such empirical models of the electron density and magnetic field configuration (Section 3.1), then we model the RM due to the nearby disk (Section 3.2), and finally in Section 3.3, we match the largest RM features with an inventory of nearby radio continuum structures that contribute to both the synchrotron emission and the RM in both hemispheres.

3.1. RMs of Pulsars with Parallax Distances

Many pulsars have approximate distances based on their DMs and models of the electron density in the disk (Yao et al. 2017, and references therein). Much more accurate distances come from a parallax, so we start with these. Using the ATNF Pulsar Catalog¹⁸ (v. 1.67, Manchester et al. 2005), we first consider pulsars in the range $10^\circ < |b| < 50^\circ$ with accurate parallax distances, $\frac{\sigma_D}{D} < 1$, where σ_D is the error in the distance, D . This gives a sample of 57 pulsars. We then separate these by height above the plane, $z = D \times \sin b$, and compute the correlation with the extragalactic RMs in the same directions, i.e., the healpix cell containing the pulsar position.

Considering the subsamples at different distances, D , and height above or below the plane, $|z|$, shown in Figure 10 and Table 4, the correlation between the extragalactic RMs and the pulsar RMs gets stronger rapidly with $|z|$ above about 0.3 kpc. For the 12 pulsars in the sample with $|z| > 1$ kpc, the Pearson correlation coefficient is a remarkable 0.97. Using a much larger sample of 296 pulsars with distances estimated from their DMs and the electron density model of Yao et al. (2017) gives weaker correlation coefficients, but still suggests that most of the RM toward the extragalactic sources is generated below $|z| < \sim 1$ kpc (Table 4). For this larger sample, the correlation coefficients vary from 0.81 to 0.88 between $0.6 < |z| < 1$ kpc. The correlation is still strong, but degraded somewhat for the second sample, perhaps because of the less precise DM distances compared with the parallax distances used for the first sample. The increasing correlation between pulsar and extragalactic RMs for pulsars with $|z|$ increasing from about 0.3 to 1 kpc agrees with the finding of Mao et al. (2012) for longitude $\ell \sim 110^\circ$ that the symmetric disk B dominates RMs for $|z| < 0.5$ kpc.

Figure 11 shows the trend of DM versus z for the pulsars used in Figure 10, along with the expected DM given by various estimates for h_e , the scale height of the ionized gas layer (Ocker et al. 2020, Table 2), assuming that the electron density,

¹⁸ https://www.atnf.csiro.au/research/pulsar/psrcat/psrcat_help.html

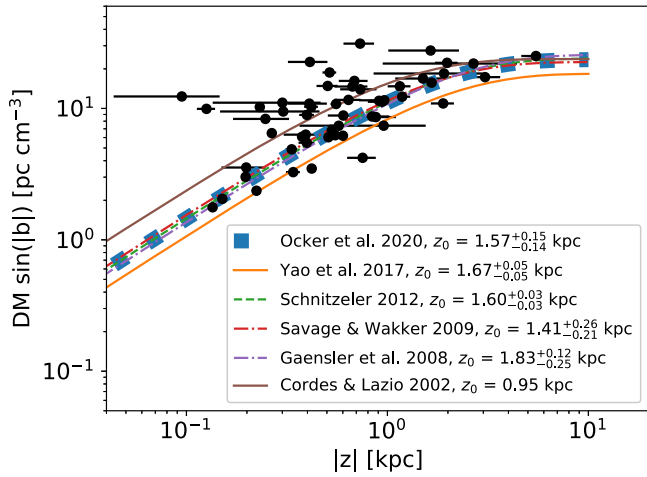


Figure 11. Dispersion measure (DM) as a function of $|z|$ for our selected 54 pulsars. Estimated trends from the literature are listed in the legend with corresponding values of the scale height of the ionized gas in the Milky Way h_e . Although the points show large scatter, the data are consistent with estimates for h_e in the range 1.0–1.8 kpc.

Table 4
RM Correlations: Pulsars versus Extragalactic Sources

Sample	Number	Pearson R	Slope
57 Pulsars with Parallax Distances, $10^\circ < b < 50^\circ$			
$0 < z < 0.3$ kpc	12	0.57	0.72
$0.3 < z < 0.6$ kpc	18	0.95	0.91
$0.6 < z < 1$ kpc	15	0.93	1.12
$1 < z < 6$ kpc	12	0.97	0.95
296 Pulsars with DM Distances, $10^\circ < b < 50^\circ$			
$0 < z < 0.3$ kpc	65	0.80	0.72
$0.3 < z < 0.6$ kpc	80	0.81	0.91
$0.6 < z < 1$ kpc	62	0.84	0.92
$1 < z < 5$ kpc	89	0.88	0.81

n_e , depends on z as

$$n_e(z) = n_{e,0} e^{-|z|/h_e} \quad (3)$$

with $n_{e,0}$ as the average midplane electron density. Recent values of h_e are ≈ 1.5 kpc. This is roughly a factor of 3 greater than the corresponding scale height of the \mathbf{B} field causing the pulsar RM. This is supported by Figure 12, which shows the average LoS magnetic field strength, $\langle B_{\parallel} \rangle = 1.232 \frac{\text{RM}}{\text{DM}}$, as a function of $|z|$ for this sample of pulsars. The curves in Figure 12 show the predictions assuming an exponential z dependence of B with different values of h_B , the magnetic field scale height (e.g., Sobey et al. 2019), and a midplane value $B(0) = 6 \mu\text{G}$ for the ordered component of the field. Most of the pulsars in our sample are between the curves for $h_B = 0.1$ kpc and $h_B = 0.5$ kpc, which is indicative of a large-scale, ordered magnetic field mostly confined to the Galactic thick disk, with a considerably smaller scale height than the thermal electrons, h_e . This result is also consistent with theoretical expectations from numerical simulations by Pakmor et al. (2018), where it is shown that, because the magnetic field strength decreases exponentially with height above the disk, the Faraday rotation

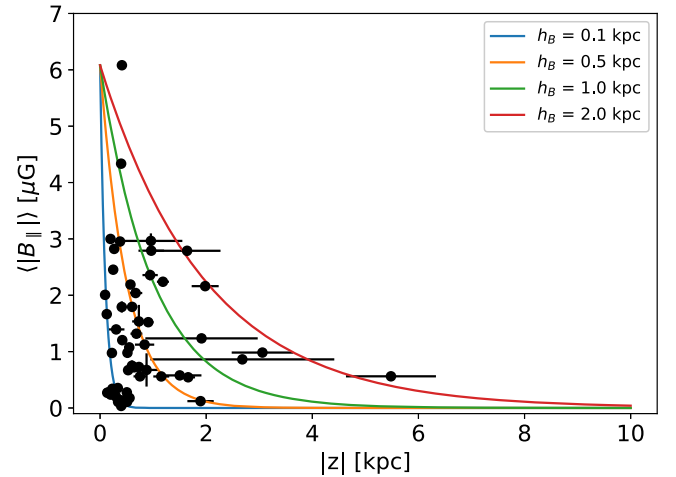


Figure 12. Correlation between the average LoS magnetic field, $\langle B_{\parallel} \rangle$, and $|z|$ for our selected 54 pulsars. Four analytical trends of the form $\langle B_{\parallel} \rangle = \langle B_{\parallel, 0} \rangle e^{-|z|/h_B}$ are overlaid as functions of the magnetic field scale height, h_B . As in Figure 11, the points are scattered over a wide range, but they are mostly consistent with $h_B < \sim 0.5$ kpc.

for an observer at the solar circle is dominated by the local environment (distance $D \sim$ a few kiloparsecs in the simulations).

The scale height of the \mathbf{B} field derived above applies only to the field as measured with Faraday rotation, i.e., the field in regions where the thermal electron density is high enough to cause significant RMs. The synchrotron emission may extend beyond the thermal electrons, because the cosmic rays and magnetic fields are not so strongly confined to the disk in regions where the mass density of the interstellar gas is low, e.g., in bubbles or chimneys of hot gas (McClure-Griffiths et al. 2000).

The RMs of pulsars with $|z| > 0.6$ kpc correlate well with extragalactic RMs. Considering the longitude dependence of the pulsar RMs, and restricting the sample to pulsars with $25^\circ < |b| < 45^\circ$ and $|z| > 0.3$ kpc, gives the points shown in Figure 13. For comparison, the results of fits of Equation (1) to the extragalactic RMs (Table 1) in these latitude ranges are shown as dashed curves. The extragalactic fits show good agreement with the pulsar points in both hemispheres.

The conclusion from this comparison with RMs of pulsars at intermediate latitudes is that they are quite consistent with the extragalactic RMs if the pulsar is more than ~ 0.6 kpc above the plane. At midlatitudes (30° – 45°), this gives distance $D > \sim 1$ kpc. There are many large structures more nearby that cast shadows on the RM sky, and we discuss them below in Section 3.3.

3.2. Comparison with Empirical Models of the Disk Field

The correlation with pulsar RMs discussed above suggests that a significant contribution to the extragalactic and GMIMS RMs may be coming from the disk field, in addition to the field in the lower halo (roughly $|z| > 0.6$ kpc). Using models for the disk field, we can predict the strength of the RMs expected at midlatitudes from the LoS path length through the disk. Figure 14 shows three models for the disk contribution, corresponding to \mathbf{B}_{disk} field models by Sun et al. (2008), Van Eck et al. (2011), and Jansson & Farrar (2012), combined with models for the thermal electron density in the disk, following

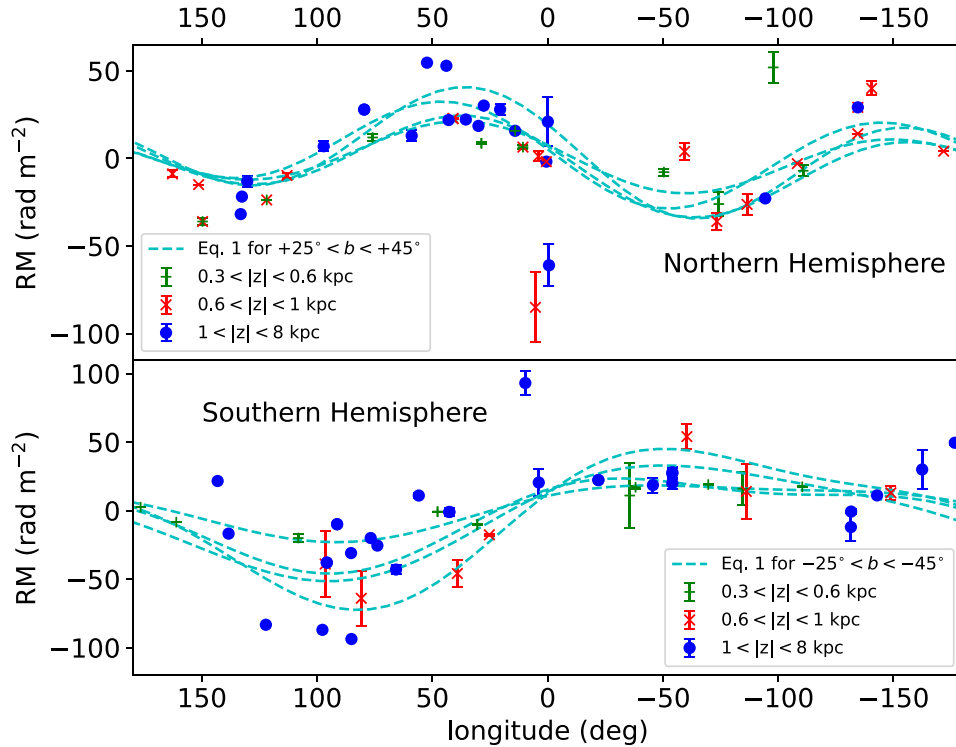


Figure 13. Rotation measure vs. longitude for pulsars with latitudes $+25^\circ \leq b \leq +45^\circ$ and $z > 0.3$ kpc (upper panel) or $-25^\circ \geq b \geq -45^\circ$ and $z < -0.3$ kpc (lower panel). For comparison, the Equation (1) predictions using the extragalactic fit parameters (Table 1) are indicated by the dashed curves. Many of the pulsars have such precisely measured RMs that the error bars are smaller than the symbols. In both hemispheres, the agreement between the extragalactic RMs and the pulsar RMs is very good, particularly for pulsars with $|z| > 0.6$ kpc.

the method for projection described in Ma et al. (2020). Since the disk field is primarily azimuthal, these necessarily give roughly $\sin(\ell + \pi)$ dependence on longitude, but they include a field reversal inside the solar circle, which adds a weak $\sin(2\ell)$ component, along with higher terms in a Fourier expansion. Overall, these disk field models are in fair agreement with the extragalactic RMs in the southern hemisphere (right-hand panel, Figure 14), but they are completely inconsistent with the RMs at positive latitudes (left-hand panel). A comparison of these disk field models with the extragalactic and diffuse RM data at midlatitudes suggests that the disk field cannot explain the $\sin(2\ell)$ behavior of the RMs at positive latitudes, but it may be sufficient to explain the $\sin(\ell + \pi)$ functions seen at negative latitudes.

An empirical approach to modeling the midlatitude RM pattern, also based on pulsar data, is that of Xu & Han (2019). Combining pulsar RMs and corresponding DMs, they find approximate $\sin(2\ell)$ and $\sin(\ell + \pi)$ functions for the intermediate latitude behavior of RM on longitude, reproduced in Figure 14 as the red curves (see their Figure 17). To explain the asymmetry between the two hemispheres, they invoke antisymmetric toroidal fields in the halo (Han et al. 1997, 1999), plus a disk field with spiral shape and two field reversals inside the solar circle (Han et al. 2006, 2018), and the nearest is at a distance of just 0.14 kpc. In Figure 14, the Xu & Han (2019) model, which includes disk and halo fields, shows the same $\sin(\ell + \pi)$ dependence as the disk models in the southern hemisphere, but it gives roughly a $\sin(2\ell)$ behavior in the north, which is much more consistent with the extragalactic and GMIMS RM data.

3.3. Nearby RM Structures

The differences between the RM patterns in the two hemispheres have been ascribed to nearby features such as the NPS (Gardner et al. 1969). For the NPS, we show in Section 2.2 that this feature alone does not generate the observed pattern of RMs in the northern hemisphere. Here we evaluate the contribution of other discrete nearby structures whose RM variations match the morphology of Stokes I synchrotron emission or $H\alpha$ emission. To illustrate this comparison, in this section, we decompose the RM surveys in spherical harmonics and display the results in orthographic projection using HEALPix tools (Górski et al. 2005).

The analysis of the functional dependence of RM on Galactic longitude, ℓ , in Section 2 by decomposing as the first few terms of a Fourier Series, Equation (1), generalizes mathematically to a decomposition in spherical harmonics, Y_l^m (e.g., Dennis & Land 2008; Drake & Wright 2020), the well-known family of orthogonal functions on a sphere. The spherical harmonic degree, l , roughly corresponds to angular scale, $\theta = 180^\circ l^{-1}$. We compute the spherical harmonics up to degree $l = 3$, which can capture dipole ($m = 1$), quadrupole ($m = 2$), and even octopole ($m = 3$) modes (i.e., $e^{3i\ell}$) on the sphere. For both the Hutschenreuter et al. (2022) map and the GMIMS map, we mask the Galactic plane for $|b| < 10^\circ$ before computing the spherical harmonics. We show the sum of the first three spherical harmonics for both maps in orthographic projection, centered on the Galactic poles, in the lower panels of Figures 15 and 16. The $\sin(2\ell)$ (north) and $\sin(\ell + \pi)$ (south) functions stand out in this representation.

The largest structures in the synchrotron sky are the Galactic loops and spurs, reviewed by Vidal et al. (2015), which stand

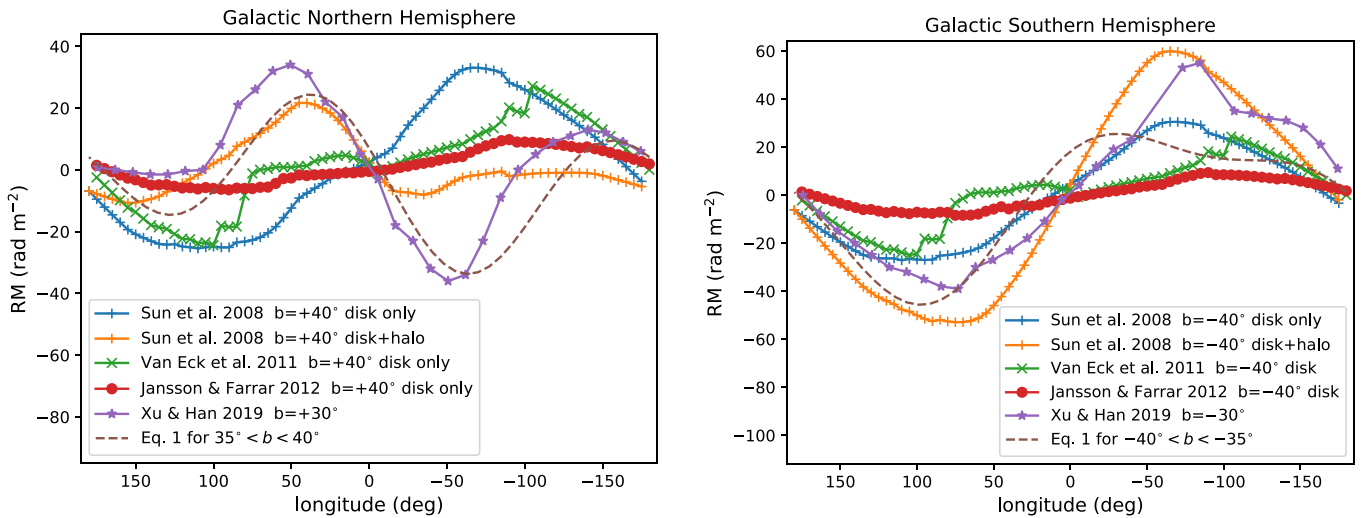


Figure 14. Models for the contribution of the disk to the RMs observed at intermediate latitudes. The left panel shows north latitudes ($b = +40^\circ$) and the right panel shows the corresponding south latitudes ($b = -40^\circ$). These are computed following the method described in Ma et al. (2020, Section 2.2). The blue and orange curves result from the model of Sun et al. (2008) for the disk component and disk plus halo, respectively. The green curve is the disk component of the model of Van Eck et al. (2011) and the red is the disk component of the model by Jansson & Farrar (2012). The recent model of the halo contribution to RMs of pulsars Xu & Han (2019) is shown in purple for $b = \pm 30^\circ$ (copied from their Figure 17). For comparison the Equation (1) fits to the extragalactic RMs for similar latitude ranges are shown by the dashed curves. The Xu & Han (2019) halo model matches the models for the GMIMS and extragalactic RMs quite well in both hemispheres, as does the Sun et al. (2008) disk-plus-halo model, but the disk-only models do not fit the RM pattern in the northern hemisphere.

out in both total synchrotron intensity (Stokes I) and polarized emission. Using the relatively sparse RM grid of the time, Simard-Normandin & Kronberg (1980) described three corresponding regions, (A), (B), and (C), which enclose the largest-scale RM features. Stil et al. (2011) revisited this description using the RM grid of Taylor et al. (2009). The areas covered by the three regions as defined by Simard-Normandin & Kronberg (1980) are as follows:

1. *Region (A)*. Loop II is a rectangle with corners $(\ell, b) = (145^\circ, -10^\circ)$ and $(170^\circ, -35^\circ)$.
2. *Region (B)*. The Gum Nebula is a circle centered at $(\ell, b) = (255^\circ, 0^\circ)$ and radius $\sim 20^\circ$ (Vallee & Bignell 1983).
3. *Region (C)*. The NPS (Loop I) is a rectangle with corners $(\ell, b) = (0^\circ, 0^\circ)$ and $(60^\circ, +60^\circ)$.

Region (A) is associated with radio continuum Loop II. The outline of Loop II, as seen in the diffuse, unpolarized synchrotron emission in the upper panel of Figure 17, follows a boundary of $RM \sim 0 \text{ rad m}^{-2}$, the white areas in Figures 15 and 16. Region (A) covers an enormous area, much of quadrants (I) and (II) in the southern hemisphere, within which the RMs are mostly negative. Nested inside Loop II is another emission feature, Loop III, which roughly mirrors the northern Loop III (center at $(\ell, b) = (124^\circ, +15.5^\circ)$ with diameter 65° ; Berkhuijsen 1971). The boundary of Loop III is associated with an increase of the absolute RM value. Thomson et al. (2021) model this region as an expanding shell, following Berkhuijsen (1973) and Vidal et al. (2015). There is an additional region of negative RM in the first Galactic quadrant of the southern hemisphere, visible in the full-resolution extragalactic map. This region is separated by a ridge of positive RM following the line of Loop II. The same positive ridge is present in the GMIMS map, but the larger area of negative of RM does not appear. However this region lies at the most southern declinations covered by the GMIMS-HBN survey.

Region (B) is associated with the Gum nebula, which is at lower latitude ($|b| < 20^\circ$) and relatively small compared with the other two, so it is unlikely to have a strong effect on the

midlatitude RMs. In contrast, regions (A) and (C) are large enough to influence the RM patterns on steradian scales.

Region (C), the NPS discussed in Section 2.3 above, appears in the first quadrant as an area of relatively uniform positive RM. In the GMIMS map, the positive region only extends as high as $b \sim 50^\circ$, whereas it extends to the north pole in the extragalactic map.

The extragalactic data show that the RM is mostly positive at southern latitudes in the third and fourth Galactic quadrants. The same is not true for the GMIMS map. Although much of the southern Galactic hemisphere could not be observed by the DRAO telescope, the observed portion of the third quadrant has mostly negative RMs.

Strong correlation can be seen between the RM and the $H\alpha$ emission from nearby H II regions, sometimes casting depolarization shadows that block the background diffuse polarization (e.g., Harvey-Smith et al. 2011; Purcell et al. 2015; Thomson et al. 2018). Regions of lower-density ionized gas traced by diffuse $H\alpha$ can strongly affect the RM. To study this effect, we plot the all-sky $H\alpha$ image of Finkbeiner (2003) in the lower panel of Figure 17. Comparing this to the full-resolution maps from both surveys (upper panels of Figures 15 and 16) reveals a correlation with $H\alpha$ emission. Latitudes $|b| < 10^\circ$ are hidden in our orthographic projection, but even so the Orion–Eridanus superbubble (Joubaud et al. 2019) shows up clearly at longitudes $180^\circ < \ell < 240^\circ$, latitudes $-45^\circ < b < -5^\circ$. There is a clear correlation with the extragalactic RMs and the Orion–Eridanus superbubble. The region itself is morphologically complex, and so is the RM distribution, but there is an enhancement in RMs along the bubble’s boundary, with primarily positive RMs there. The correlation with RM is far less clear in the GMIMS data. While there appear to be correlated RM enhancements along the $H\alpha$ filaments, the GMIMS RM structure does not match the $H\alpha$ as well as the extragalactic RMs do. The maps combining just the low-order Y_l^m terms (lower panels of Figure 16) show that the GMIMS RM is mostly negative in the Orion–Eridanus area. The difference between the GMIMS and extragalactic RMs in this area suggests that much

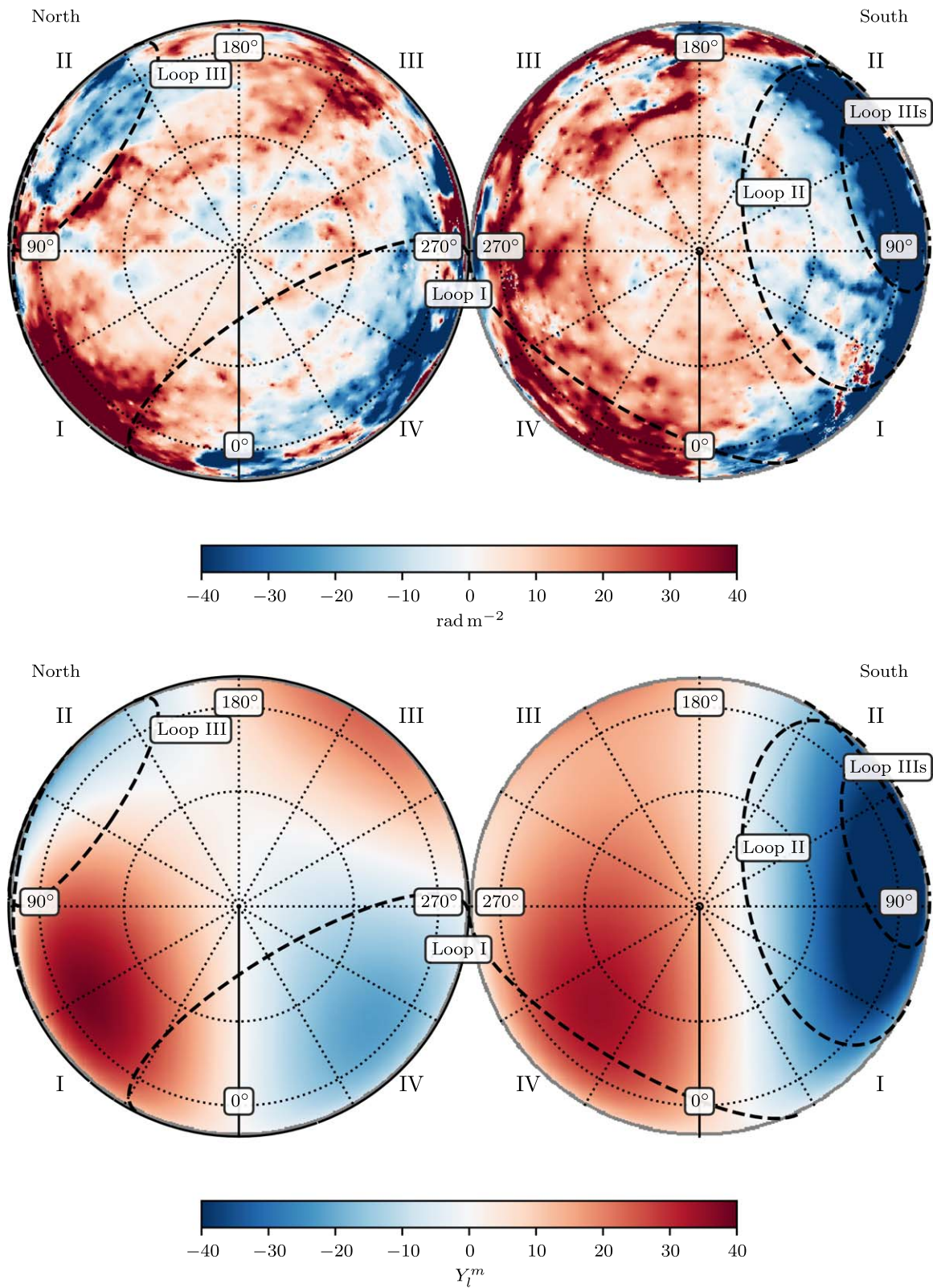


Figure 15. Upper: the extragalactic RM map of Hutschenreuter et al. (2022) in orthographic projection, centered on the Galactic poles. The left panel shows the northern hemisphere, the right panel shows the south, with circles of constant latitude at $b = \pm 30^\circ$ and $\pm 60^\circ$. Lower: the spherical harmonic expansion of the Hutschenreuter et al. (2022) RM distribution with $l_{\max} = 3$. We overlay the positions of nearby radio continuum loops (Vidal et al. 2015) and label the Galactic quadrants by Roman numerals on both panels. As these are images of the sky, parity is reversed compared with the ordinary face-on view of the Galactic plane seen from above the northern hemisphere.

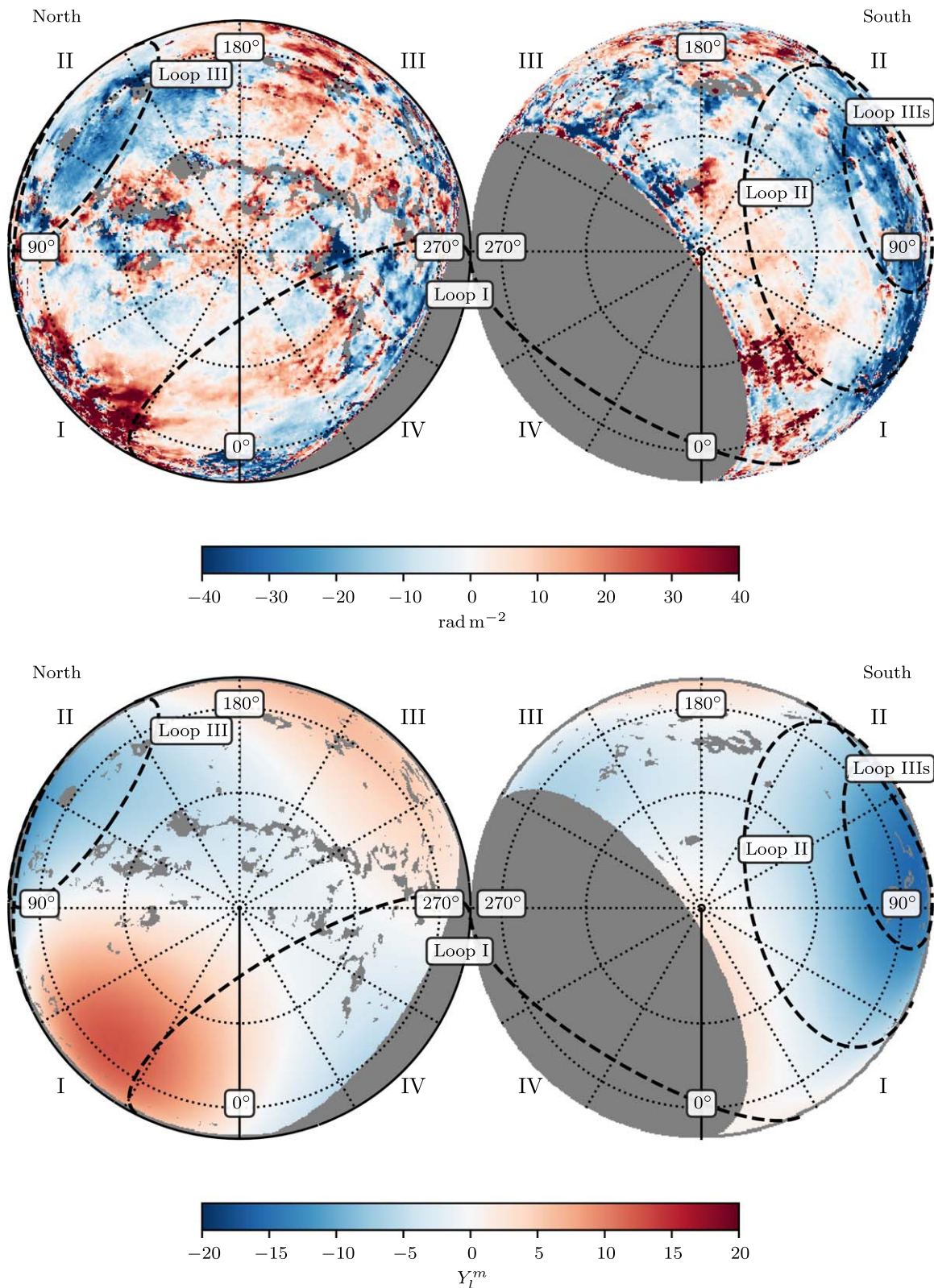


Figure 16. The upper panels show the Wolleben et al. (2021) map of the GMIMS RMs in orthographic projection. The lower panels show the spherical harmonic expansion, as in Figure 15. The radio continuum loops discussed in the text are indicated as in Figure 15. The gray patches are areas where the signal-to-noise is too low to allow calculation of the first moment of the Faraday spectrum.

of the diffuse synchrotron emission is coming from the vicinity of the superbubble itself, and from the foreground.

In the northern Galactic hemisphere, the two RM maps show good agreement. The strongest common feature is the region of

negative RM encircled by Loop III in the second quadrant. The appearance of this loop is very similar to that of Loop II in the south, with diffuse Stokes I emission following a line of $\text{RM} \sim 0 \text{ rad m}^{-2}$. In the full-resolution versions of both maps,

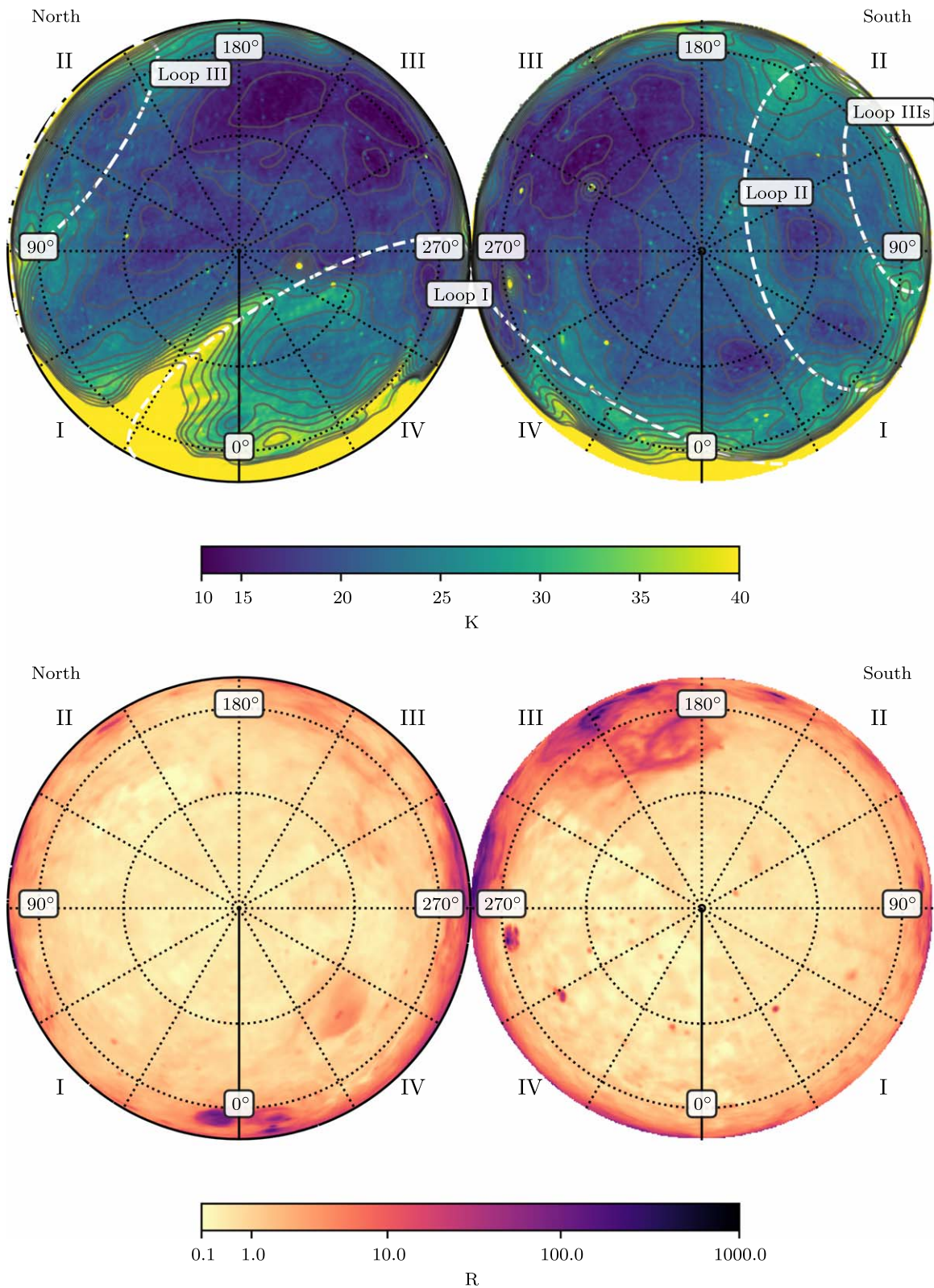


Figure 17. The upper panels show Stokes I emission at 408 MHz (destriped; Haslam et al. 1982; Remazeilles et al. 2015). The lower panels show the $H\alpha$ emission from SHASSA, VTSS, and WHAM (Finkbeiner 2003). Alignment and overlays are the same as Figure 15.

there is a clear ridge of positive RM, which sharply changes to negative across the boundary of Loop III. Loop I (the NPS) crosses the intermediate latitude range at $l \approx 30^\circ$. The strongest positive RM features in the GMIMS map match the morphology of the spur. In both the GMIMS and the extragalactic

maps, however, there is a sharp change in the strength of the RM along the ridge of the NPS (Sun et al. 2015). The distance to the high-latitude component of Loop I has been constrained to ~ 0.1 kpc using starlight polarization (Panopoulou et al. 2021).

In summary, Loop I does not appear to contribute strongly to the $\sin(2\ell)$ pattern in the northern Galactic hemisphere (as shown in Section 2.3 above). Loops II, III, and IIIs do make significant contributions to the RMs in both surveys. No strong distance constraints have been placed on these loops, but their huge angular sizes and the corresponding Stokes I emission suggests that they are local features. Orion–Eridanus also has a large-scale effect on the RM sky.

The $\sin(2\ell)$ and $\sin(\ell + \pi)$ structure of the RM sky in the inner Galactic quadrants (first and fourth) does not appear to be associated with any local discrete structures. The Y_l^m decompositions show that the RM pattern appears antisymmetric about the Galactic plane at longitudes $-90^\circ < \ell < +90^\circ$. It is when we include the outer quadrants (second and third) that the asymmetry appears, along with the association with local features. It is therefore possible that the RM structure from the global magnetic field is antisymmetric about the Galactic plane, but the antisymmetric pattern is obscured in the outer Galaxy by the effects of nearby objects.

4. Self-consistent Field Configurations Based on RM Maps

The discussion in Section 3 shows that the difference between the $\sin(2\ell)$ and $\sin(\ell + \pi)$ variation of RM with longitude in the northern and southern hemispheres is not easily explained by the effects of nearby discrete structures such as H II regions or radio continuum loops. The very good correlation with RMs of pulsars with parallax distances shows that most of the Faraday rotation in the extragalactic sample occurs in the thick disk or lower halo, below $|z| \sim 1$ kpc. Outside of the thin disk, $|z| \sim 0.1$ kpc, the field configuration must change dramatically and differently in the two hemispheres, to explain the disagreement between the disk \mathbf{B} field models shown in Figure 14, and the intermediate latitude extragalactic and GMIMS RM results. How the field changes with z , and why it changes so differently in the north and south, is the fundamental question considered in this section.

To go beyond the empirical models of the \mathbf{B} field, like those illustrated in Figure 14, requires a physical approach to the generation and maintenance of the magnetic field as a solution to the plasma equations (e.g., Ferrière & Terral 2014). Dynamo configurations provide the preferred model because dynamo processes in the interstellar medium can both amplify the field (the small-scale dynamo) and sustain a global mean field, i.e., the $\alpha - \Omega$ dynamo (Beck 2015). To try to explain the RM variation with ℓ described in Section 2, we consider the scale-invariant models of Henriksen (2017) and Henriksen et al. (2018), which solve the magnetohydrodynamic equations including diffusion and a velocity field in the medium, in a form that assumes scale invariance and solutions that are self-similar in time. Various velocity fields in the gas are considered by Henriksen et al. (2018), and different amounts of diffusion. These models do not separate disk and halo contributions to the field; they make a continuous, global solution to the plasma equations and hence to the vector potential and finally the magnetic field.

Here we explore whether a large angular-scale model of the Galactic magnetic field can reproduce the main features described in Section 2, namely the following:

1. asymmetry across the Galactic plane,
2. a $\sin(2\ell)$ RM pattern in the north,
3. a $\sin(\ell + \pi)$ RM pattern in the south,

4. the amplitudes of the two patterns differ by a factor of 2, with the stronger amplitude in the south.

In this section, we show that a dynamo-based model can be found that displays these general features. We have not achieved an exact match between our model and the data, and we deliberately leave this to future work. Our goal here is simply to demonstrate that dynamo models are strongly relevant to understanding the observed patterns in the RM sky. Following the approach of West et al. (2020, Section 3), we start with a combination of M0 (axisymmetric) and M1 (bisymmetric) spiral modes, each either positive or negative in radial direction, and each either dipolar (continuous field across the midplane) or quadrupolar, i.e., symmetric field on either side of the midplane (Sokoloff & Shukurov 1990). Combining just these two simplest spiral modes makes possible a diverse set of field configurations, some of which are asymmetric between the hemispheres, as seen in Figure 18.

For the \mathbf{B} field configuration that matches each spiral pattern, we use combinations of dynamo models developed by Henriksen (2017) and Henriksen et al. (2018), and subsequently applied to modeling the edge-on spiral galaxy NGC 4631 by Woodfinden et al. (2019). We use the best-fit case from Woodfinden et al. (2019) as a test case for this work. Different approaches start more or less from the same set of dynamo equations, but some use numerical techniques involving the solution of partial differential equations, and some use other semianalytic approximations, such as assuming a *zero* z approximation. The advantage of scale invariance is that it allows a quick survey of the possibilities based on algebraic equations and analytic solutions, and most importantly, it allows a coherent treatment of the disk and halo fields together. The dynamo models used in this work do not separate the disk field from the halo field. Rather, the two components are a result of the same scale-invariant dynamo modes.

We solve the dynamo equations for the $M=0$ and $M=1$ cases, where M is the spiral mode, using a grid that has $n_x = 64$, $n_y = 64$, and $n_z = 32$ pixels, corresponding to a single hemisphere of the model magnetic field of a galaxy, and using a physical scale of 0.625 kpc pixel $^{-1}$ (i.e., 64 pixels corresponds to 40 kpc). The model has no small-scale structure, and so this relatively coarse resolution is sufficient. The coordinate system defines the plane of the model galaxy to be parallel to the x - y plane, with the origin at its Galactic center. The z -axis is perpendicular to the plane, with $z > 0$ toward the northern hemisphere. We scale the average strength of the output magnetic field of the $M=0$ mode to be $1 \mu\text{G}$. We then scale the $M=1$ mode to have the same average power, and thus the same average RM, as the $M=0$ mode.

We find the solution for the dynamo equation for the vector potential (Henriksen 2017, Equation (1)) for points where $z > 0$, and then assume either dipolar or quadrupolar symmetry across the disk of the galaxy to calculate points where $z < 0$. We integrate the coherent field using a low-resolution Healpix projection $N_{\text{side}} = 64$, corresponding to roughly 1° pixels. This angular resolution corresponds to a physical scale perpendicular to the LoS that is roughly 0.2 kpc at a distance of 10 kpc.

We place the observer inside of this grid, at a position similar to the Sun's position in the Galaxy, i.e., $(x, y, z) = (-8, 0, 0)$ kpc. We then use the Hammurabi code (Waelkens et al. 2009) to compute the RM for an observer embedded inside this magnetic field geometry. The RM is computed by integrating volume elements along lines of sight through a grid where each

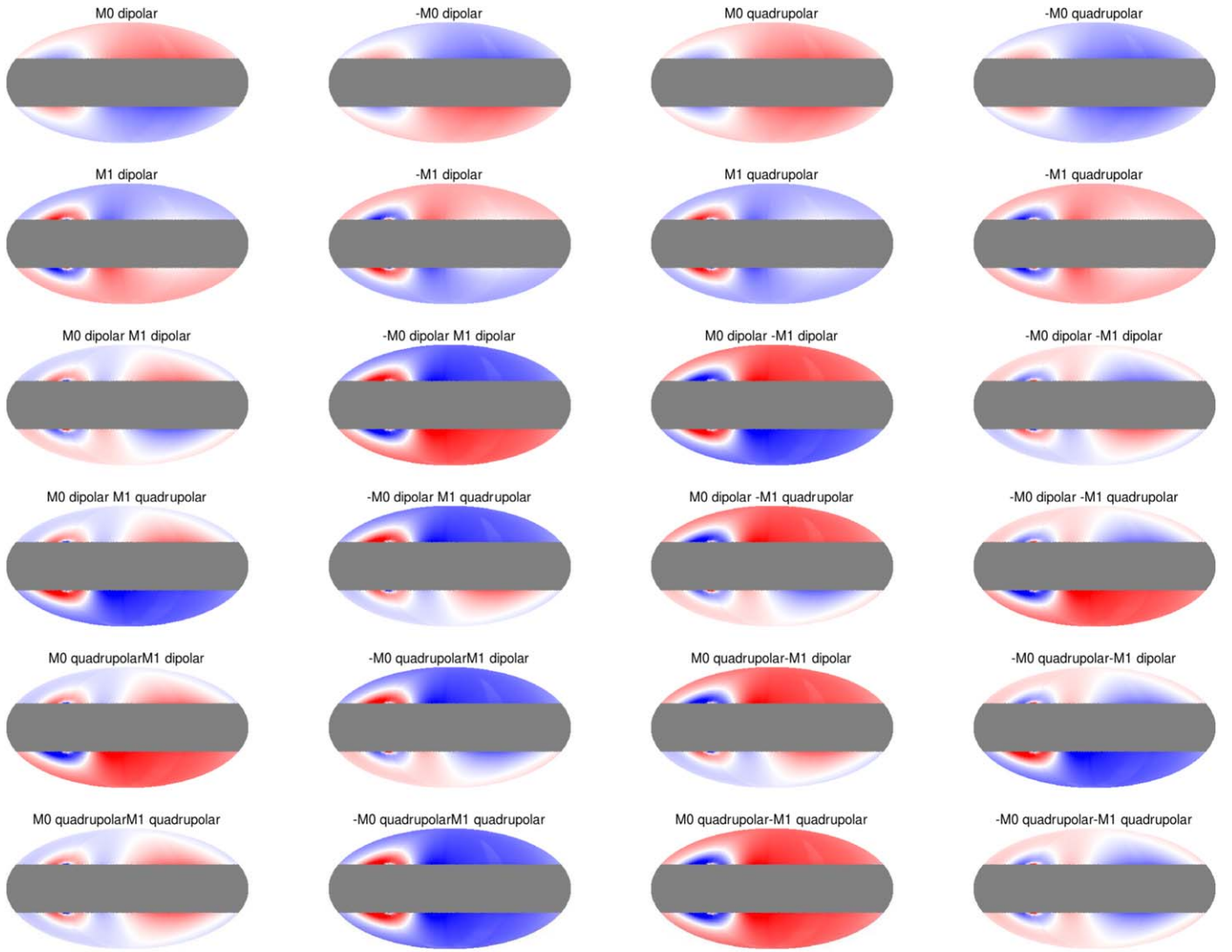


Figure 18. Simulated RM maps showing the $M = 0$ and $M = 1$ modes, each with \pm dipolar and quadrupolar symmetry. The two top rows show these modes individually. The lower rows show all 16 combinations thereof. The case of $-M0$ dipolar added to $-M1$ quadrupolar, in the fourth row and rightmost column, is reproduced in Figure 19.

element, i , contributes an increment of RM calculated by $RM_i = 0.81 n_e B_{i,\parallel} \Delta r$. Here n_e is the thermal electron density of the halo, which we assume to have a constant value of 0.01 cm^{-3} , and Δr is the element size (0.625 kpc).

The output is a Healpix image (Górski et al. 2005) of the RM across the sky, which can be compared with the extragalactic RM data. We mask latitudes below $|b| = 30^\circ$ because we cannot adequately display them on this image, and because our primary interest is at higher latitudes. The top two rows of Figure 18 show the $M = 0$ and $M = 1$ modes, each with dipolar or quadrupolar symmetry. The following rows show all 16 combinations of the $M = 0$ plus $M = 1$ modes, with equal amplitudes, positive or negative, in each case. In these panels, we have rotated the center point of the longitude axis by 100° clockwise to more closely resemble the appearance of the pattern we observe in the real data. This rotation is equivalent to changing the viewing position within the model galaxy, i.e., the (x, y) coordinates, but while maintaining the same radial distance, i.e., $r = \sqrt{x^2 + y^2} = 8 \text{ kpc}$. Here we can see that the $M = 0$ or $M = 1$ mode alone cannot reproduce a $\sin(2\ell)$ pattern. However, the combination of $-\mathbf{B}_{M=1}$ (dipolar) added

to $-\mathbf{B}_{M=1}$ (quadrupolar) can crudely reproduce all of the observed features, including the asymmetry across the plane. This model is shown in larger format in Figure 19. Slices through the model at latitudes $+35^\circ < b < +40^\circ$ and $-45^\circ < b < -40^\circ$ corresponding to Figures 2 and 6 are shown in Figure 20. The \mathbf{B} field on three planes that make sections through the Galaxy is shown in Figure 21 to illustrate the complexity of the field in this $-M0-M1$ model. Although the model has not been adjusted to fit the data, and clearly adjustment is needed as seen by the mismatch in Figure 20, the fact that the two hemispheres in this model give such different overall RM patterns motivates further work.

5. Discussion

Comparing the RM surveys based on diffuse emission (GMIMS) and the foreground derived from extragalactic source RMs, the data in Section 2 show that the midlatitude regions, roughly $10^\circ < |b| < 50^\circ$ in both hemispheres, are where a large-scale, coherent picture emerges. Near the plane, $|b| < 10^\circ$, and at both poles, $|b| > 50^\circ$, the two surveys do not correlate, either because the path lengths sampled by the two

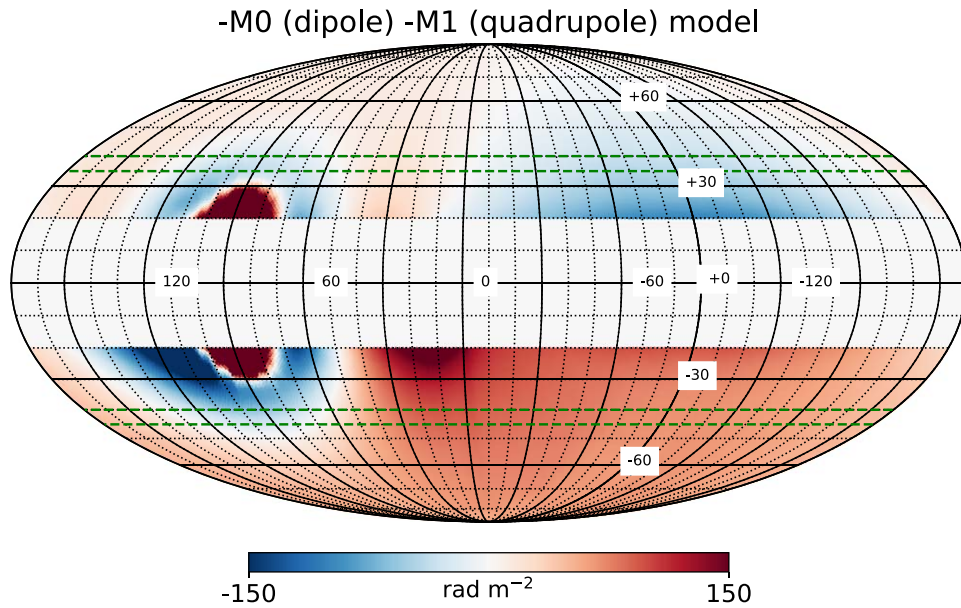


Figure 19. The preferred model RM distribution resulting from a halo field configuration including $-M0$ dipolar and $-M1$ quadrupolar components. The model is arbitrarily rotated in longitude. Latitudes $-20^\circ < b < +20^\circ$ are blanked. Latitude ranges used to compute the azimuth dependence shown in Figure 20 are indicated by dashed green lines.

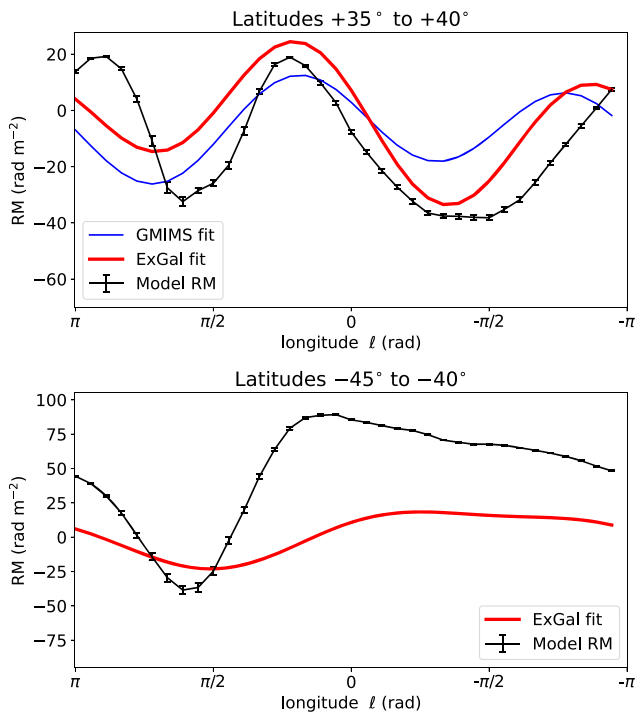


Figure 20. Constant latitude binned slices through the $-M0$ – $M1$ model. The upper panel covers latitudes $+35^\circ < b < +40^\circ$; the red and blue curves are copied from the upper panel of Figure 2. The lower panel is for $-45^\circ < b < -40^\circ$ corresponding to Figure 6. Error bars show the scatter of values in each longitude bin, which are necessarily small because of the low angular resolution of the model.

techniques are different or because of different resolutions, both in angle and on the Faraday spectrum, $\delta\phi$. However, at midlatitudes the very good agreement between the two quite different observational methods indicates that the Milky Way magnetic field can be traced reliably with RM surveys of either type.

If there were a one-to-one correspondence between GMIMS and extragalactic RMs, i.e., slope of 1 in Figure 8, that would indicate that the Galactic synchrotron emission all comes from behind the entire volume of Faraday rotating medium. In regions where this is not the case, a comparison of the two RM maps gives information on how these two media are mixed along every LoS.

To understand the values of the amplitude ratios and correlation slopes displayed in Figure 8, we consider a Burn slab (Burn 1966) as described in Section 2.4. Such a mixed rotating and emitting region has a finite width, $\Delta\varphi$, in the Faraday spectrum, because emission from different points along the LoS undergoes different amounts of rotation. For a Burn slab, the detected polarization angle is a linear function of the wavelength squared, just as it is for a background point source that undergoes rotation due to the same uniform magnetic field along the LoS. The RM derived from that slope is half the value of the corresponding point-source RM, leading to a ratio of 2, shown by the upper blue line in Figure 8. For the GMIMS-HBN survey, the RMSF is broader than $\Delta\varphi$ for any realistic slab at intermediate latitudes, so the slab is unresolved in φ , with a single Faraday depth peak near the center of $\Delta\varphi$, giving approximately half the value of the total RM of the slab.

If the slab is in the foreground, and the synchrotron emission extends farther along the LoS than the Faraday rotating medium, then the ratio of the extragalactic RM to the diffuse RM can be less than 2. The ratio is 1 in the extreme where the slab becomes simply a foreground screen of rotating plasma with all the emission coming from beyond the screen.

The two points in Figure 8 above $b = +40^\circ$ that give slopes of 0.71 ± 0.14 and 0.56 ± 0.16 (see the lower right panel of Figure 2) are revealing; a value less than 1 in this ratio implies a field reversal along the LoS, beyond the diffuse emission. If there are one or more sign changes in the magnetic field component along the LoS, then the interpretation of the RM ratios can get much more complicated. In that case, the diffuse RM could be arbitrarily high, either positive or negative, and the extragalactic RM could be zero, or vice versa, giving C_2

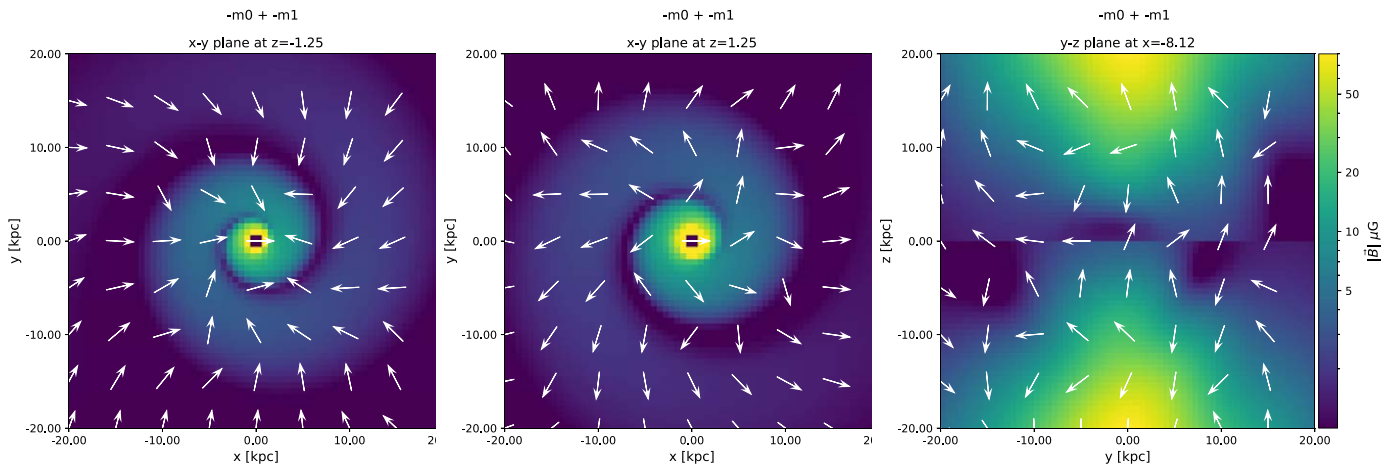


Figure 21. Examples of the \mathbf{B} field configuration in the $-M0$ (dipolar) and $-M1$ (quadrupolar) model. The left and middle panels show the field direction projected on planes parallel to the midplane, displaced above and below midplane by 1.25 kpc. The right panel shows the field on a plane perpendicular to the midplane, through a position ($x = -8.1$ kpc, $y = 0$, $z = 0$) normal to the radial direction, roughly corresponding to the position of the observer for the computation of the RM Figures 18–20. The \mathbf{B} field model is for a generic spiral galaxy; it has not been fitted to the Milky Way, so the scales on the axes are representative. Unlike Figures 18–20, the field is not integrated along the line of sight nor projected on the sky; these panels merely illustrate sections through the model. The background color shows the magnitude of the field ($|\mathbf{B}|$), with a logarithmic scale. The field is neither symmetric nor antisymmetric about the midplane.

ratios of zero or $\pm \infty$, or anything in between. Modeling the Faraday spectrum with better resolution would be needed to interpret the RMs in that case (e.g., Bracco et al. 2022; Erceg et al. 2022, Appendix C). This suggests that at positive latitudes we may be looking through a field reversal that is several hundred parsecs above the midplane. The absence of correlation between the GMIMS and extragalactic survey RM at the highest latitudes could be explained if the diffuse emission comes from both behind and in front of the reversal.

The simplest and most striking result of the analysis of the RMs in Section 2 is that the typical values of the RM in the Galactic southern hemisphere are bigger than those in the north. In Table 1 and Figure 3, the C_1 term has values of 50–60 rad m^{-2} for $-5^\circ > b > -30^\circ$, dropping smoothly to $\sim 30 \text{ rad m}^{-2}$ at $b = -40^\circ$. This is not clear in the GMIMS data because of the sparse coverage of southern declinations, but for the extragalactic data on the lower right-hand panel of Figure 3, the blue curve at the southern latitudes is a factor of 2 above the red curve, and a factor of 4 above the blue curve at the corresponding northern latitudes. The different amplitudes of the RMs in the two hemispheres are expected in the $-M0$ – $M1$ model of Section 4 (Figures 19 and 20).

In the south, the correspondence of the main negative RM area with the insides of Loop II and Loop III is striking in the right panels of Figures 15 and 16, in the range $60^\circ < \ell < 120^\circ$. Positive RMs dominate the whole longitude range $180^\circ < \ell < 360^\circ$, but in the Orion–Eridanus region, they are the strongest, mostly at southern latitudes but reaching into the north in the longitude range $240^\circ < \ell < 260^\circ$. These two structures by themselves may cause the very large values of RM in the south that are not seen in the north. Thus the northern hemisphere may be a window to the halo field ($|z| > 0.3$ kpc) whereas in the south the RMs are dominated by structures in the nearby disk. So both the effect of synchrotron loops with distances less than ~ 1 kpc (Section 3) and the global models including the halo field ($|z| > 0.5$ kpc; Section 4) may be needed to understand the difference between the RM patterns in the northern and southern hemispheres.

This synthesis of the two frameworks, on the one hand, nearby structures on large angular scales, and, on the other, a global halo-field pattern, is supported by the ratios of values of

C_2 and the correlation slopes shown in Figure 8. All the southern hemisphere slopes are consistent with a value of 2, suggesting that the synchrotron emission and the Faraday rotation are mixed in a single emitting–rotating medium. The lower values in the northern hemisphere, between 1 and 2 but mostly closer to 1, indicate that there the diffuse synchrotron emission is mostly coming from beyond the medium that causes the Faraday rotation, thus at distances greater than ~ 1 kpc. Distance estimates to more interstellar dust clouds (Lallement et al. 2018; Pelgrims et al. 2020), and observations of the three-dimensional structure in the \mathbf{B} field around these clouds (Tahani et al. 2019, 2022a, 2022b) are rapidly improving our understanding of the field in the nearby disk. As larger surveys become available, e.g., POSSUM (Gaensler et al. 2010; Anderson et al. 2021) and SPICE-RACS (A. J. M. Thomson et al. 2022, in preparation), these large-scale and small-scale RM studies can be unified.

6. Conclusions

Comparing the RM map of the Milky Way derived from large samples of extragalactic source RMs with the first-moment map derived from the GMIMS Faraday depth spectra of the diffuse synchrotron emission shows that these two data sets often give very different results. Where they agree is on the large angular scales, at intermediate Galactic latitudes. Surprisingly, the patterns that show up in both surveys are neither symmetric nor antisymmetric between the northern and southern Galactic hemispheres. In the north, there is a strong $\sin(2\ell)$ pattern in the RMs between $b = +10^\circ$ and $b = +50^\circ$. The pattern is closely, but not precisely, aligned with the Galactic center, i.e., $20^\circ > \phi_2 > 5^\circ$; see Figure 9. In contrast, the southern hemisphere shows a $\sin(\ell + \pi)$ pattern, with the π phase offset indicating that RMs in the first and second Galactic quadrants are mostly negative, while in the third and fourth quadrants they are mostly positive. Again, the pattern is aligned closely with longitude 0° . Pulsar RMs match these patterns when we consider only pulsars well above and below the thin disk ($|z| > \sim 0.6$ kpc).

The question raised by comparison of GMIMS and extragalactic RMs is as follows: why are the northern and southern

hemispheres so different? In Sections 3 and 4, we take a first step toward a coherent picture of the global magnetic field configuration in the disk and halo of the Milky Way.

Large angular-scale, nearby structures like the radio continuum loops show morphological correspondence with RM features. Expanding the RMs in low-order spherical harmonics makes this correspondence clearer, as shown in Figures 15 and 16. Loops II, III, and IIIs trace the boundaries of large areas of negative RMs, and Loop I, i.e., the NPS, has high positive RM. The boundary of the Orion–Eridanus superbubble is traced by positive RMs. To the extent that distances are known, these loops and bubbles are within 1 kpc of the Sun (West et al. 2021, and references therein), with the possible exception of parts of Loop I (Lallement 2022).

If the midlatitude RM patterns cannot be explained entirely by these nearby structures, then they may help to determine the pattern of the \mathbf{B} field in the lower Galactic halo ($|z| > \sim 0.5$ kpc). If the vertical z -component of the \mathbf{B} field is continuous at $z=0$, as in a dipole (M0) configuration, then it is hard to reconcile the asymmetry between the hemispheres in their RM patterns. Adding a quadrupole (M1) field, which has anti-symmetry between the hemispheres, can introduce a discontinuity in combined B_z at $z=0$, so it helps to match the data, as in the $-M0$ – $M1$ model discussed in Section 4.

At low latitudes ($|b| < 5^\circ$), the RM pattern is more complicated (reviewed by Han 2017). The \mathbf{B} field in the disk is primarily spiral or azimuthal, but with at least one field reversal just a few hundred parsecs inside the solar circle (e.g., Simard-Normandin & Kronberg 1980; Sofue & Fujimoto 1983; Rand & Kulkarni 1989; Weisberg et al. 2004; Xu & Han 2019). An azimuthal field naturally gives a $\sin(\ell)$ pattern, and a nearby reversal introduces a $\sin(2\ell)$ and higher-order terms (Van Eck et al. 2011) that may be connected with the inter-arm halo field described by Mao et al. (2012).

An attractive conjecture is that the field reversal seen in the disk just ~ 0.15 – 0.3 kpc inside the solar circle at $z=0$ might move to larger Galactic radius at positive z , so that it passes directly above the solar circle at $z \sim 0.3$ kpc. Ordog et al. (2017) have shown that the Sagittarius Arm reversal ($\ell \sim 52^\circ$ to 72°) is not cylindrical (see also Ma et al. 2020). The latitude of the reversal boundary is a linear function of longitude, with slope about 0.5, implying that its height above the plane, z , increases linearly with Galactic radius. A similar radial slope of the nearby field reversal would be a natural explanation for the $\sin(2\ell)$ pattern in the RMs at midlatitudes in the northern Galactic hemisphere.

Nearby edge-on spiral galaxies show “X-shaped” \mathbf{B} fields in their halos; see Ferrière & Terral (2014), Krause et al. (2020) reviewed by Beck (2015, Section 4.13). A particularly dramatic example is NGC 4631 (Mora-Partiarroyo et al. 2019), which shows field reversals in its northern halo. The pattern has been modeled with dynamo components similar to those illustrated in Figure 18 (Woodfinden et al. 2019). This is what the local field reversal would look like if it extends radially at high z . The smooth shift in the longitude of zero-phase as a function of latitude (Figure 9) could indicate a variation of the pitch angle of the reversal with height above the plane, z .

The ratio between the Galactic and extragalactic RMs suggests that, in the northern hemisphere, the synchrotron emission is mostly beyond the Faraday rotating medium, whereas the two are spatially mixed in the south (Section 5). Moving beyond a single homogeneous slab or screen geometry leads to more complex models for the juxtaposition of the rotating and

emitting regions. An example is the model of Basu et al. (2019) that includes the effects of random fields. The much finer resolution, $\delta\varphi$, in the Faraday spectra observed by LOFAR at $\lambda \sim 1$ m gives sufficient precision to motivate such detailed interpretations (Sobey et al. 2019; Bracco et al. 2022; Erceg et al. 2022). The broad RMSF of the GMIMS-HBN observations does not justify a similar fine-scale analysis of the Faraday spectrum in these data.

When the GMIMS HBN (DRAO) survey is supplemented by a low-band survey in the northern hemisphere, then models of the propagation of the polarized radiation through the magnetoionic medium can be improved. Better sampling of the extragalactic RM will be provided by POSSUM (Gaensler et al. 2010; Anderson et al. 2021), a much larger radio polarization survey than all previous observations put together. Similarly, the parameters of the dynamo models of the magnetic field structures described briefly in Section 4 can be adjusted to better fit the RM data from all three kinds of polarized emission: pulsars, extragalactic sources, and the diffuse synchrotron radiation.

The authors are grateful to Bryan Gaensler, Wolfgang Reich, and an anonymous referee for helpful comments on the manuscript. A.B. acknowledges support from the European Union’s Horizon 2020 research and innovation program through the Marie Skłodowska-Curie grant agreement No. 843008 and from the European Research Council through the advanced grant MIST (FP7/2017-2022, No. 742719). J.L.H. is supported by the National Natural Science Foundation of China (grant Nos. 11988101, 11833009). A.S.H. is supported by a Natural Sciences and Engineering Research Council (NSERC) Discovery grant. A.O. is supported by the Dunlap Institute for Astronomy and Astrophysics at the University of Toronto. A.E. and V.J. acknowledge support from the Croatian Science Foundation for project IP-2018-01-2889 (LowFreqCRO).

Software: this research made use of SciPy (Virtanen et al. 2020); NumPy (van der Walt et al. 2011); Matplotlib, a Python library for publication quality graphics (Hunter 2007); and Astropy,¹⁹ a community-developed core Python package for Astronomy (Astropy Collaboration et al. 2013).

Appendix A

The Effect of Binning the RM Values Before Correlation

Grouping the values of RM from the extragalactic and GMIMS surveys into bins 5° – 10° on a side and then computing the median of the values in each bin greatly reduces the scatter in the points in Figures 2 and 7. The bin size has very little effect on the results of fitting for the constants in Equation (1). To confirm the robustness of the results in Table 1, we repeat the analysis of Section 2 using all integer factors of 360 between 24 and 90 for the number of longitude bins for each 5° latitude band. Two examples are shown in Figure 22, with 24 and 90 bins respectively, for latitudes $+35^\circ < b < +40^\circ$, corresponding to the upper panel of Figure 2. The upper panel of Figure 22 has 24 bins of width 15° ; the lower panel has 90 bins of width 4° . The fitted functions have quite similar values for the amplitudes and phases of both the $\sin(\ell)$ and $\sin(2\ell)$ terms. Considering the full latitude range $20^\circ < b < 50^\circ$ where the fitted value of C_2 is greater than five times the error gives Figure 23. The fitted values of C_2 , i.e., the amplitude of the $\sin(2\ell)$ term, are plotted for each latitude using longitude bins

¹⁹ <http://www.astropy.org>

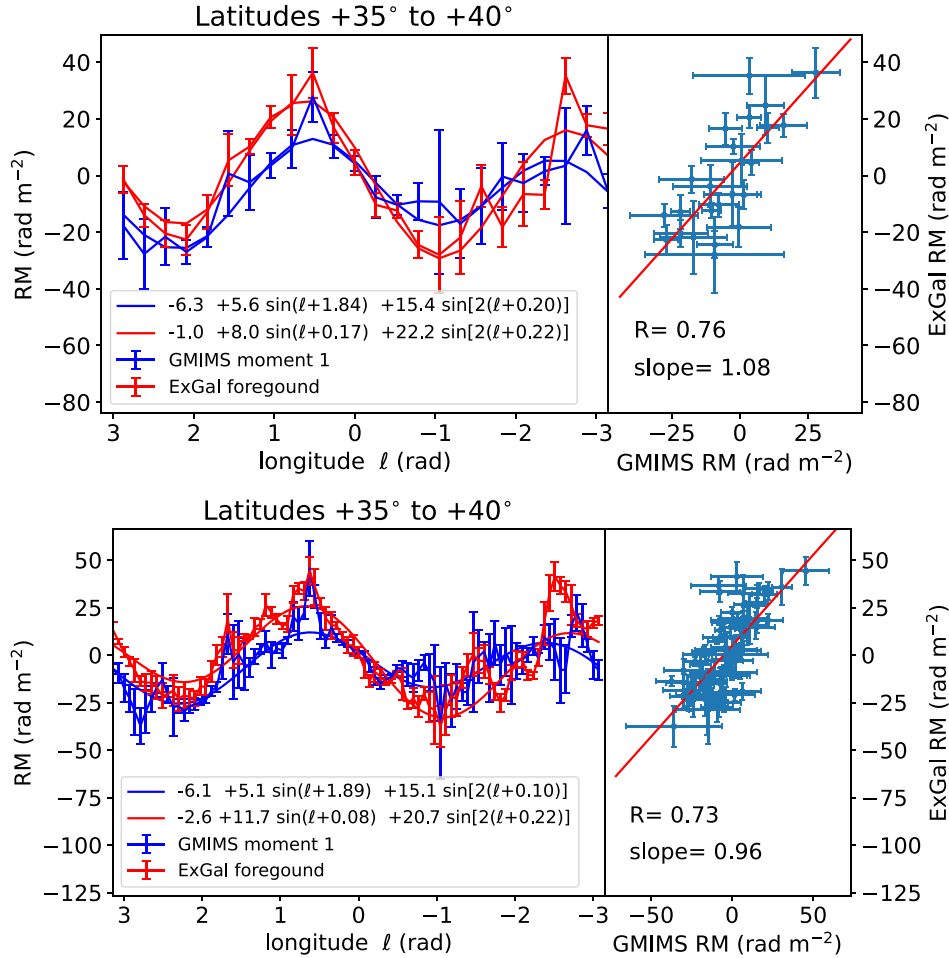


Figure 22. Illustration of the effect of changing the bin width in longitude from 15° (24 bins, top panel) to 4° (90 bins, lower panel). Although there is more structure in the data on scales of a few degrees with the smaller bins, the results from fitting sine curves are changed only slightly.

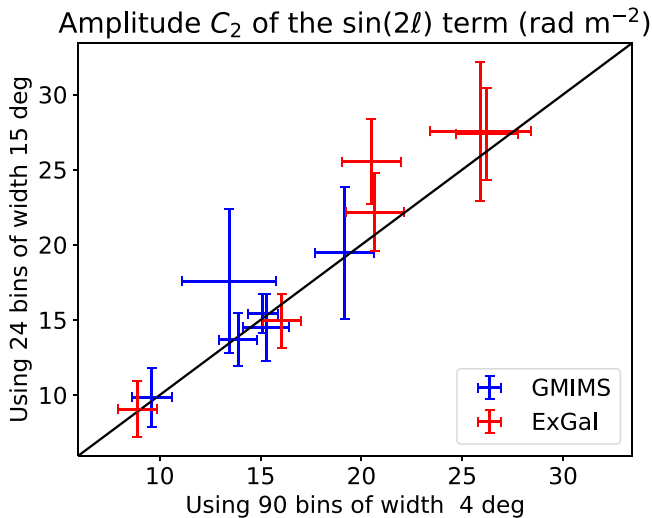


Figure 23. Comparing the fitted values of coefficient C_2 (Equation (1)) at different latitudes for different bin widths, 4° and 15°, as in Figure 22. Only latitudes giving values of $C_2 > 5\sigma$ are shown. For all but one point, the results agree within error bars of $\pm 1\sigma$. From this and similar comparisons with many different bin widths, we conclude that the bin size has minimal effect on the least-squares fitting in Section 2.

of 4° versus 15°. The results are quite consistent, with only one of the 12 points showing more than 1σ difference.

Decreasing the size of the bins has a moderate effect on the correlation between the extragalactic and GMIMS values of RM. This is shown in Figure 24. Each trace shows the result of computing correlations like those shown in Figure 4, for different bin widths from 15° to 4°. For most latitudes, the correlation coefficient, R , decreases as the bins get narrower, from roughly 0.75 for bins $\sim 10^\circ$ wide or more, down to about 0.70 for bin widths of 4°–5°. Although the effect is small, the fact that the narrower bins show less correlation suggests that the large angle patterns are well correlated between the two surveys, while the structure in RMs at angles less than about 5° is less well correlated. This result might be expected if the small angular-scale variations come from structures that cover narrow intervals along the LoS. The two surveys weight the polarized emission from different distances differently, so small features have different effects in the two.

In addition to checking the effect of the bin widths, it is interesting to check whether the smoothing and interpolation of the extragalactic RMs to make the continuous RM function of Hutschenreuter et al. (2022) has a significant effect on the fitting results. For this we use the catalog of Taylor et al. (2009)

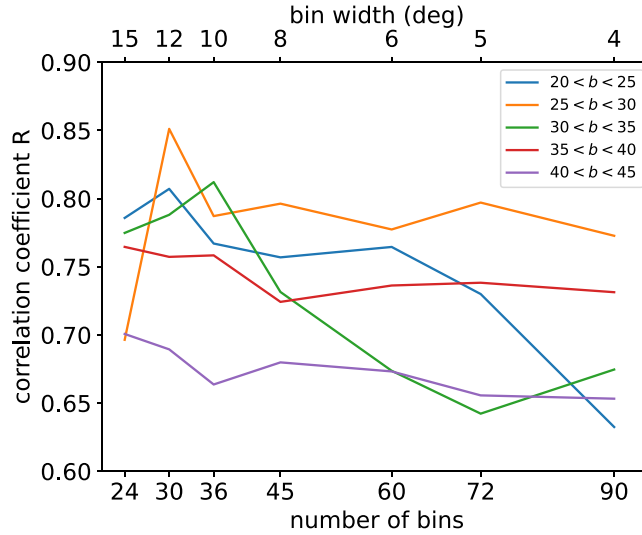


Figure 24. The correlation between RMs from the two surveys as a function of the bin widths. There is a small but significant reduction in the correlation coefficient as the bins get smaller.

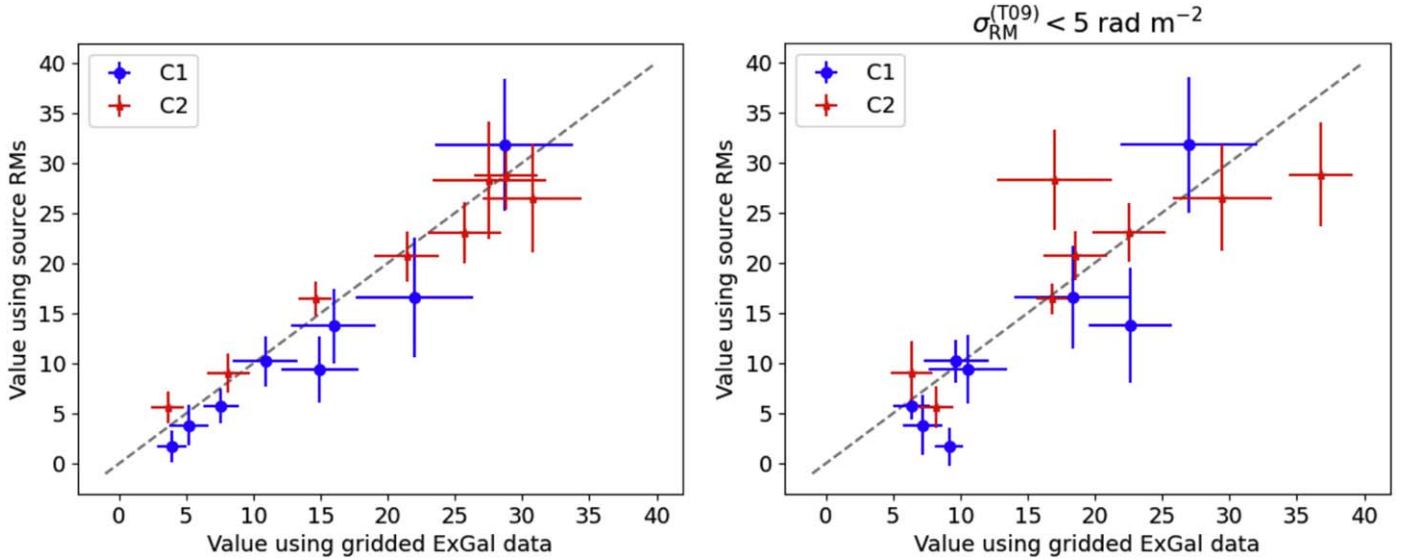


Figure 25. Comparing the fitted values of coefficients C_1 and C_2 (Equation (1)) at northern latitudes ($15^\circ < b < 55^\circ$) for 10° bins using the gridded extragalactic RMs vs. binning the extragalactic sources directly from Taylor et al. (2009). The left panel uses all sources with equal weighting. The right panel uses only the sources with the highest precision in RM, i.e., those with measurement error $\sigma_{\text{RM}} < 5 \text{ rad m}^{-2}$.

and bin the RMs of the sources directly, then compute the median of the RMs in each bin. The result is shown on the left panel of Figure 25. The values of the coefficients C_1 and C_2 are consistent within the error bars, except for those points that have poorly determined values of the constants (less than 5σ) from the least-squares fitting (Equation (1)). The right panel of Figure 25 shows a similar result for a smaller sample of extragalactic sources, only those with nominal high precision ($\sigma_{\text{RM}} < 5 \text{ rad m}^{-2}$) in the RM measurements by Taylor et al. (2009). Reducing the size of the sample has the effect of degrading the correlation with the binned result, in spite of the higher precision of the individual measurements.

Appendix B

Chi-square, Goodness of Fit, and the RM Distribution Function

The quality of the least-squares fits of the median RMs in each longitude bin is considered here, using the method of

reduced chi-square (χ_ν^2), following the technique described in Barlow (1989, Section 8.3). We define χ^2 as

$$\chi^2 = \sum_{i=1}^n \frac{[y_i - f(\ell_i)]^2}{\sigma_i^2} \quad (\text{B1})$$

where n is the number of data points (in this case, $n=36$ except at latitudes where there are no samples in one or more bins because they are below the decl. limit of the GMIMS survey), and y_i is the median of the binned values of the RM at each longitude, ℓ_i . The rms errors of the measured values are σ_i , and the fitted function $f(\ell_i)$ has the form of Equation (1), with the values of the five parameters, C_0 , C_1 , C_2 , ϕ_1 , and ϕ_2 as described in Section 2.1. Dividing by the number of degrees of freedom, $\nu = n - k$, where $k = 5$ is the number of parameters in the model. This gives the reduced chi-square statistic:

$$\chi_\nu^2 = \frac{\chi^2}{\nu}. \quad (\text{B2})$$

Table 5
Reduced Chi-squared Results

Latitude Range	GMIMS		ExGal	
	χ^2_ν	Ψ^2_ν	χ^2_ν	Ψ^2_ν
$-60^\circ < b \leq -55^\circ$	1.2 ± 0.4	3.5 ± 0.3	2.5 ± 0.3	6.5 ± 0.2
$-55^\circ < b \leq -50^\circ$	1.8 ± 0.4	3.8 ± 0.3	2.2 ± 0.3	12.4 ± 0.2
$-50^\circ < b \leq -45^\circ$	1.7 ± 0.4	4.6 ± 0.3	1.3 ± 0.3	7.1 ± 0.2
$-45^\circ < b \leq -40^\circ$	0.5 ± 0.4	1.8 ± 0.3	2.1 ± 0.3	7.2 ± 0.2
$-40^\circ < b \leq -35^\circ$	0.8 ± 0.4	1.5 ± 0.3	2.6 ± 0.3	11.4 ± 0.2
$-35^\circ < b \leq -30^\circ$	0.8 ± 0.3	1.9 ± 0.3	2.9 ± 0.3	15.1 ± 0.2
$-30^\circ < b \leq -25^\circ$	0.7 ± 0.3	2.3 ± 0.3	2.4 ± 0.3	13.1 ± 0.2
$-25^\circ < b \leq -20^\circ$	0.6 ± 0.3	1.7 ± 0.3	1.8 ± 0.3	9.1 ± 0.2
$-20^\circ < b \leq -15^\circ$	0.8 ± 0.3	1.8 ± 0.3	2.8 ± 0.3	8.4 ± 0.2
$-15^\circ < b \leq -10^\circ$	0.5 ± 0.3	0.8 ± 0.3	3.3 ± 0.3	6.6 ± 0.2
$-10^\circ < b \leq -5^\circ$	0.6 ± 0.3	1.0 ± 0.3	1.3 ± 0.3	4.8 ± 0.2
$-5^\circ < b \leq 0^\circ$	0.8 ± 0.3	2.4 ± 0.3	0.7 ± 0.3	2.8 ± 0.2
$0^\circ < b \leq 5^\circ$	0.5 ± 0.3	1.2 ± 0.3	0.9 ± 0.3	2.6 ± 0.2
$5^\circ < b \leq 10^\circ$	0.4 ± 0.3	1.6 ± 0.3	1.7 ± 0.3	4.7 ± 0.2
$10^\circ < b \leq 15^\circ$	1.1 ± 0.3	3.2 ± 0.3	1.7 ± 0.3	4.1 ± 0.2
$15^\circ < b \leq 20^\circ$	0.5 ± 0.3	2.7 ± 0.3	1.8 ± 0.3	4.9 ± 0.2
$20^\circ < b \leq 25^\circ$	0.7 ± 0.3	1.9 ± 0.3	1.8 ± 0.3	4.9 ± 0.2
$25^\circ < b \leq 30^\circ$	1.2 ± 0.3	2.9 ± 0.3	1.7 ± 0.3	8.4 ± 0.2
$30^\circ < b \leq 35^\circ$	0.9 ± 0.3	4.5 ± 0.3	2.6 ± 0.3	9.1 ± 0.2
$35^\circ < b \leq 40^\circ$	0.8 ± 0.3	6.4 ± 0.2	2.9 ± 0.3	10.3 ± 0.2
$40^\circ < b \leq 45^\circ$	1.3 ± 0.3	5.9 ± 0.2	1.5 ± 0.3	9.0 ± 0.2
$45^\circ < b \leq 50^\circ$	1.2 ± 0.3	5.0 ± 0.2	1.6 ± 0.3	4.3 ± 0.2
$50^\circ < b \leq 55^\circ$	0.9 ± 0.3	2.4 ± 0.2	1.8 ± 0.3	4.7 ± 0.2
$55^\circ < b \leq 60^\circ$	0.9 ± 0.3	1.7 ± 0.2	1.6 ± 0.3	4.0 ± 0.2

If the fitted function, f , completely describes the underlying variation between the data points, y_i , (but not the errors) then we expect $\chi^2_\nu \sim 1$. Under ideal conditions (Andrae et al. 2010), the excess of χ^2_ν above 1 can be interpreted as a probability that the fitted function fully explains the underlying variation among the measured values, as a statistical test of null hypothesis. Even though these conditions do not apply here, it is useful to consider the quality of the fitted functions for each latitude, with parameters given in Table 1, by computing χ^2_ν and comparing it to a value that would give 10% probability, $P=0.1$, that the data are fully described by the model, and that the residuals are purely due to the errors, σ_i , in the data points.

As Barlow (1989) points out, for large ν ($\nu > \sim 30$), the quantity $\sqrt{2\chi^2}$ is distributed roughly as a Gaussian with mean value $\sqrt{2\nu - 1}$, and standard deviation equal to 1. With this approximation, the probability P gives χ^2_ν using the inverse of the error function, erf^{-1} (`erfinv` in SCIPY.SPECIAL), as follows:

$$\chi^2_\nu \simeq \frac{[\sqrt{2\nu - 1} + \sqrt{2} \cdot \text{erf}^{-1}(1 - 2P)]^2}{2\nu} \quad (\text{for } \nu > \sim 30). \quad (\text{B3})$$

This gives $\chi^2_\nu < 1.33$ for $P < 0.10$ with $\nu = 31$ (the more precise SCIPY routine `chdtri` gives 1.34). The model must be linear in the fitted parameters to allow interpretation of P as a probability, but Equation (1) is not linear in the phases, ϕ_1 and ϕ_2 . So the conclusion that $P = 0.1$ or 10% probability of the residuals exceeding this value by chance, corresponding to the 1.33 threshold in χ^2_ν , is only for comparison purposes.

Table 5 gives values for χ^2_ν for all latitude fits, for both the GMIMS and extragalactic data, corresponding to Table 1.

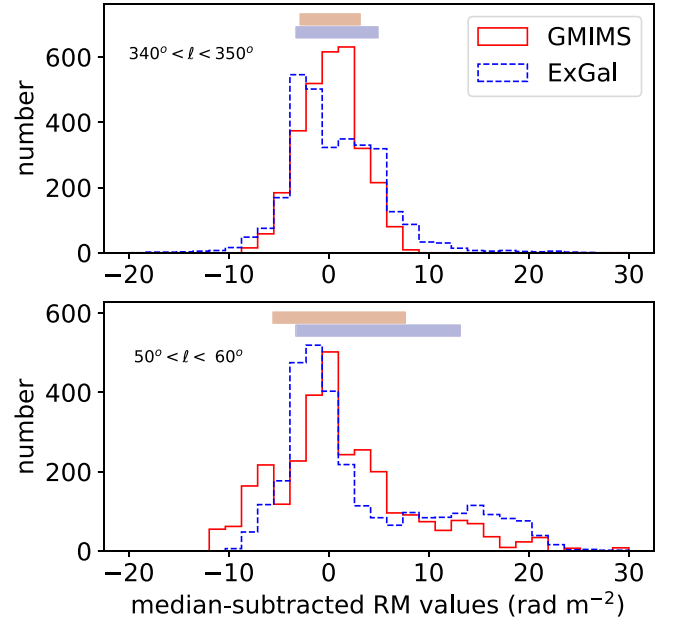


Figure 26. Two examples of the distributions of values in longitude bins, both for the range $35^\circ < b < 40^\circ$, with the GMIMS histogram in red and the extragalactic in blue. The upper panel shows the distribution of samples in the longitude bin from $340^\circ \ell < 350^\circ$, the lower panel shows the same for the bin from $50^\circ < \ell < 60^\circ$ that includes part of the North Polar Spur. In both cases, the medians have been subtracted from the values, so that all the histograms have zero median. The rectangles at the top show the range from the 16th to the 84th percentiles, which we use to determine $\pm 1\sigma$ for the error bars in Figure 2 and for the determination of χ^2_ν in Table 5.

Errors on the χ^2_ν values in Table 5 are simply $\sqrt{2/\nu}$ assuming that the variance of χ^2 is $2 \cdot \nu$. Of particular interest is the range of northern latitudes where the $\sin 2\ell$ term dominates the fitted function, for both the GMIMS and extragalactic data, i.e., $+20 < b < +50$. The GMIMS data are consistent with $\chi^2_\nu = 1.0$ for this range. The extragalactic values of χ^2_ν are greater than one, typically by more than their errors. This suggests that the data could be better fitted with a function with more parameters, e.g., more terms in a Fourier series. This is not surprising since the $\sin \ell$ and $\sin 2\ell$ functions cannot model the variations of RM on angular scales smaller than about $\frac{\pi}{2}$ radians, but there is a great deal of structure in the RM distribution on all angular scales (e.g., Haverkorn et al. 2008). For comparison, Table 5 shows χ^2_ν for a different model, given by simply removing the mean value of the RMs at each latitude, i.e.,



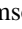











$$\Psi^2_\nu = \sum_{i=1}^n \frac{[y_i - \bar{y}]^2}{\sigma_i^2} \quad (\text{B4})$$

where \bar{y} is the mean of the y_i values, and for this case $\nu = 35$. In all cases, $\Psi^2_\nu > \chi^2_\nu$, typically by a factor of 3 to 5, which shows that fitting functions with the form of Equation (1) is well justified, although further fitting on smaller angular scales would also be justified for the extragalactic data in particular. For the GMIMS data, there is also structure on angular scales smaller than 1 radian, as can be seen by the contrast between the upper and lower panels for Figure 16, so adding more terms to Equation (1) would certainly decrease the values of χ^2_ν . The fact that these values are already less than 1 in Table 5 suggests that the error bars on the data points, i.e., the errors on the median RM values in each bin, have been overestimated.

A fundamental source of misinterpretation in the application of the χ^2 statistic is the possibility that the errors of the fitted data points, σ_i , do not reflect variances of Gaussian distributions. Studying the distributions of the points in the bins shows that sometimes they are roughly normally distributed and sometimes not. Figure 26 shows two typical cases, both taken from longitude bins for the latitude range $35^\circ < b < 40^\circ$. The upper panel shows distributions that are approximately normal, but the lower panel shows a case for which both samples show a long positive-going tail. In some other bins, one or both distributions are bimodal. A proper statistical analysis of goodness of fit to a model should be done using Monte Carlo methods based on the probability distributions themselves, as in the Markov Chain Monte Carlo analysis of Thomson et al. (2019).

The rich texture of the RM patterns on the sky causes the non-Gaussian RM distributions in the bins. It also contributes to the relatively high values of the χ^2_ν for the extragalactic data in Table 5. Modeling the RM patterns of both surveys on angular scales smaller than ~ 1 radian is beyond the scope of this paper. As surveys with a greater areal density of RMs become available, the effective angular resolution of the RM maps will improve, allowing more detailed modeling of structures in the Galactic magnetic field on a wide range of scales.

ORCID iDs

John M. Dickey  <https://orcid.org/0000-0002-6300-7459>
 Jennifer West  <https://orcid.org/0000-0001-7722-8458>
 Alec J. M. Thomson  <https://orcid.org/0000-0001-9472-041X>
 T. L. Landecker  <https://orcid.org/0000-0003-1455-2546>
 A. Bracco  <https://orcid.org/0000-0003-0932-3140>
 E. Carretti  <https://orcid.org/0000-0002-3973-8403>
 J. L. Han  <https://orcid.org/0000-0002-0274-3092>
 A. S. Hill  <https://orcid.org/0000-0001-7301-5666>
 Y. K. Ma  <https://orcid.org/0000-0003-0742-2006>
 S. A. Mao  <https://orcid.org/0000-0001-8906-7866>
 A. Ordog  <https://orcid.org/0000-0002-2465-8937>
 Jo-Anne C. Brown  <https://orcid.org/0000-0003-4781-5701>
 K. A. Douglas  <https://orcid.org/0000-0003-3320-2728>
 R. Kothes  <https://orcid.org/0000-0001-5953-0100>

References

- Anderson, C. S., Heald, G. H., Eilek, J. A., et al. 2021, *PASA*, 38, e020
 Andrae, R., Schulze-Hartung, T., & Melchior, P. 2010, arXiv:1012.3754
 Astropy Collaboration, Robitaille, T. P., Tollerud, E. J., et al. 2013, *A&A*, 558, A33
 Barlow, R. J. 1989, *Statistics. A Guide to the use of Statistical Methods in the Physical Sciences* (New York: Wiley)
 Basu, A., Fletcher, A., Mao, S. A., et al. 2019, *Galax*, 7, 89
 Beck, R. 2015, *A&ARv*, 24, 4
 Berkhuijsen, E. M. 1971, *A&A*, 14, 359
 Berkhuijsen, E. M. 1973, *A&A*, 24, 143
 Bracco, A., Ntormousi, E., Jelić, V., et al. 2022, *A&A*, 663, A37
 Brentjens, M. A., & de Bruyn, A. G. 2005, *A&A*, 441, 1217
 Brown, J. C., Haverkorn, M., Gaensler, B. M., et al. 2007, *ApJ*, 663, 258
 Burn, B. J. 1966, *MNRAS*, 133, 67
 Cordes, J. M., & Lazio, T. J. W. 2002, arXiv:astro-ph/0207156
 Dennis, M. R., & Land, K. 2008, *MNRAS*, 383, 424
 Dickey, J. M., Landecker, T. L., Thomson, A. J. M., et al. 2019, *ApJ*, 871, 106
 Drake, K. P., & Wright, G. B. 2020, *JCoPh*, 416, 109544
 Erceg, A., Jelić, V., Haverkorn, M., et al. 2022, *A&A*, 663, A7
 Ferrière, K. 2016, *JPhCS*, 767, 012006
 Ferrière, K., & Terral, P. 2014, *A&A*, 561, A100
 Ferrière, K., West, J. L., & Jaffe, T. R. 2021, *MNRAS*, 507, 4968
 Finkbeiner, D. P. 2003, *ApJS*, 146, 407
 Gaensler, B. M., Landecker, T. L., Taylor, A. R. & POSSUM Collaboration 2010, AAS Meeting Abstracts, 215, 470.13
 Gaensler, B. M., Madsen, G. J., Chatterjee, S., & Mao, S. A. 2008, *PASA*, 25, 184
 Gardner, F. F., Morris, D., & Whiteoak, J. B. 1969, *AuJPh*, 22, 79
 Górski, K. M., Hivon, E., Banday, A. J., et al. 2005, *ApJ*, 622, 759
 Han, J. L. 2001, *Ap&SS*, 278, 181
 Han, J. L. 2017, *ARA&A*, 55, 111
 Han, J. L., Manchester, R. N., Berkhuijsen, E. M., & Beck, R. 1997, *A&A*, 322, 98
 Han, J. L., Manchester, R. N., Lyne, A. G., Qiao, G. J., & van Straten, W. 2006, *ApJ*, 642, 868
 Han, J. L., Manchester, R. N., & Qiao, G. J. 1999, *MNRAS*, 306, 371
 Han, J. L., Manchester, R. N., van Straten, W., & Demorest, P. 2018, *ApJS*, 234, 11
 Han, J. L., & Qiao, G. J. 1994, *A&A*, 288, 759
 Harvey-Smith, L., Madsen, G. J., & Gaensler, B. M. 2011, *ApJ*, 736, 83
 Haslam, C. G. T., Salter, C. J., Stoffel, H., & Wilson, W. E. 1982, *A&AS*, 47, 1
 Haverkorn, M. 2015, in *Magnetic Fields in Diffuse Media*, Astrophysics and Space Science Library, ed. A. Lazarian, E. M. de Gouveia Dal Pino, & C. Melioli, Vol. 407 (Berlin: Springer), 483
 Haverkorn, M., Brown, J. C., Gaensler, B. M., & McClure-Griffiths, N. M. 2008, *ApJ*, 680, 362
 Henriksen, R. N. 2017, *MNRAS*, 469, 4806
 Henriksen, R. N., & Irwin, J. 2021, *ApJ*, 920, 133
 Henriksen, R. N., Woodfinden, A., & Irwin, J. A. 2018, *MNRAS*, 476, 635
 Hunter, J. D. 2007, *CSE*, 9, 90
 Hutschenreuter, S., Anderson, C. S., Betti, S., et al. 2022, *A&A*, 657, A43
 Hutschenreuter, S., & Enßlin, T. A. 2020, *A&A*, 633, A150
 Indrani, C., & Deshpande, A. A. 1999, *NewA*, 4, 33
 Jaffe, T. R. 2019, *Galax*, 7, 52
 Jansson, R., & Farrar, G. R. 2012, *ApJ*, 757, 14
 Joubaud, T., Grenier, I. A., Ballet, J., & Soler, J. D. 2019, *A&A*, 631, A52
 Krause, M., Irwin, J., Schmidt, P., et al. 2020, *A&A*, 639, A112
 Lallement, R. 2022, arXiv:2203.01312
 Lallement, R., Capitanio, L., Ruiz-Dern, L., et al. 2018, *A&A*, 616, A132
 Landecker, T. L., Reich, W., Reid, R. I., et al. 2010, *A&A*, 520, A80
 Lenc, E., Gaensler, B. M., Sun, X. H., et al. 2016, *ApJ*, 830, 38
 Ma, Y. K., Mao, S. A., Ordog, A., & Brown, J. C. 2020, *MNRAS*, 497, 3097
 Manchester, R. N., Hobbs, G. B., Teoh, A., & Hobbs, M. 2005, *AJ*, 129, 1993
 Mao, S. A., McClure-Griffiths, N. M., Gaensler, B. M., et al. 2012, *ApJ*, 755, 21
 McClure-Griffiths, N. M., Dickey, J. M., Gaensler, B. M., et al. 2000, *AJ*, 119, 2828
 McKimven, R. 2021, PhD thesis, University of Toronto
 Mora-Partiarroyo, S. C., Krause, M., Basu, A., et al. 2019, *A&A*, 632, A11
 Ocker, S. K., Cordes, J. M., & Chatterjee, S. 2020, *ApJ*, 897, 124
 Oppermann, N., Junklewitz, H., Greiner, M., et al. 2015, *A&A*, 575, A118
 Oppermann, N., Junklewitz, H., Robbers, G., et al. 2012, *A&A*, 542, A93
 Ordog, A. 2020, *PhD thesis*, University of Calgary
 Ordog, A., Booth, R., Van Eck, C., Brown, J.-A., & Landecker, T. 2019, *Galax*, 7, 43
 Ordog, A., Brown, J. C., Kothes, R., & Landecker, T. L. 2017, *A&A*, 603, A15
 Pakmor, R., Guillet, T., Pfrommer, C., et al. 2018, *MNRAS*, 481, 4410
 Panopoulou, G. V., Dickinson, C., Readhead, A. C. S., Pearson, T. J., & Peel, M. W. 2021, *ApJ*, 922, 210
 Pelgrims, V., Ferrière, K., Boulanger, F., Lallement, R., & Montier, L. 2020, *A&A*, 636, A17
 Purcell, C. R., Gaensler, B. M., Sun, X. H., et al. 2015, *ApJ*, 804, 22
 Rand, R. J., & Kulkarni, S. R. 1989, *ApJ*, 343, 760
 Remazeilles, M., Dickinson, C., Banday, A. J., Bigot-Sazy, M. A., & Ghosh, T. 2015, *MNRAS*, 451, 4311
 Riseley, C. J., Galvin, T. J., Sobey, C., et al. 2020, *PASA*, 37, e029
 Simard-Normandin, M., & Kronberg, P. P. 1980, *ApJ*, 242, 74
 Sobey, C., Bilous, A. V., Griebmeier, J. M., et al. 2019, *MNRAS*, 484, 3646
 Sofue, Y., & Fujimoto, M. 1983, *ApJ*, 265, 722
 Sokoloff, D., & Shukurov, A. 1990, *Natur*, 347, 51
 Sokoloff, D. D., Bykov, A. A., Shukurov, A., et al. 1998, *MNRAS*, 299, 189
 Spoelstra, T. A. T. 1984, *A&A*, 135, 238
 Stil, J. M., & Taylor, A. R. 2007, *ApJL*, 663, L21
 Stil, J. M., Taylor, A. R., & Sunström, C. 2011, *ApJ*, 726, 4
 Sun, X. H., Landecker, T. L., Gaensler, B. M., et al. 2015, *ApJ*, 811, 40
 Sun, X.-H., & Reich, W. 2010, *RAA*, 10, 1287
 Sun, X. H., Reich, W., Waelkens, A., & Enßlin, T. A. 2008, *A&A*, 477, 573

- Tahani, M., Glover, J., Lupypciw, W., et al. 2022a, *A&A*, **660**, L7
- Tahani, M., Lupypciw, W., Glover, J., et al. 2022b, *A&A*, **660**, A97
- Tahani, M., Plume, R., Brown, J. C., Soler, J. D., & Kainulainen, J. 2019, *A&A*, **632**, A68
- Taylor, A. R., Stil, J. M., & Sunstrum, C. 2009, *ApJ*, **702**, 1230
- Thomson, A. J. M., Landecker, T. L., Dickey, J. M., et al. 2019, *MNRAS*, **487**, 4751
- Thomson, A. J. M., Landecker, T. L., McClure-Griffiths, N. M., et al. 2021, *MNRAS*, **507**, 3495
- Thomson, A. J. M., McClure-Griffiths, N. M., Federrath, C., et al. 2018, *MNRAS*, **479**, 5620
- Tribble, P. C. 1991, *MNRAS*, **250**, 726
- Vallee, J. P., & Bignell, R. C. 1983, *ApJ*, **272**, 131
- van der Walt, S., Colbert, S. C., & Varoquaux, G. 2011, *CSE*, **13**, 22
- Van Eck, C. L., Brown, J. C., Stil, J. M., et al. 2011, *ApJ*, **728**, 97
- Van Eck, C. L., Haverkorn, M., Alves, M. I. R., et al. 2019, *A&A*, **623**, A71
- Vidal, M., Dickinson, C., Davies, R. D., & Leahy, J. P. 2015, *MNRAS*, **452**, 656
- Virtanen, P., Gommers, R., Oliphant, T. E., et al. 2020, *NatMe*, **17**, 261
- Waelkens, A., Jaffe, T., Reinecke, M., Kitaura, F. S., & Enßlin, T. A. 2009, *A&A*, **495**, 697
- Weisberg, J. M., Cordes, J. M., Kuan, B., et al. 2004, *ApJS*, **150**, 317
- West, J. L., Henriksen, R. N., Ferrière, K., et al. 2020, *MNRAS*, **499**, 3673
- West, J. L., Landecker, T. L., Gaensler, B. M., Jaffe, T., & Hill, A. S. 2021, *ApJ*, **923**, 58
- Wolleben, M., Landecker, T. L., Douglas, K. A., et al. 2021, *AJ*, **162**, 35
- Wolleben, M., Landecker, T. L., Hovey, G. J., et al. 2010, *AJ*, **139**, 1681
- Woodfinden, A., Henriksen, R. N., Irwin, J., & Mora-Partiarroyo, S. C. 2019, *MNRAS*, **487**, 1498
- Xu, J., & Han, J.-L. 2014, *RAA*, **14**, 942
- Xu, J., & Han, J. L. 2019, *MNRAS*, **486**, 4275
- Yao, J. M., Manchester, R. N., & Wang, N. 2017, *ApJ*, **835**, 29